

## RESEARCH ARTICLE

# Major surface melting over the Ross Ice Shelf part II: Surface energy balance

Xun Zou<sup>1,2</sup>  | David H. Bromwich<sup>1,2</sup>  | Alvaro Montenegro<sup>2</sup>  |  
Sheng-Hung Wang<sup>1</sup>  | Lesheng Bai<sup>1</sup>

<sup>1</sup>Polar Meteorology Group, Byrd Polar and Climate Research Center, The Ohio State University, Columbus, Ohio

<sup>2</sup>Atmospheric Sciences Program, Department of Geography, The Ohio State University, Columbus, Ohio

## Correspondence

X. Zou, Polar Meteorology Group, Byrd Polar and Climate Research Center, The Ohio State University, 1090 Carmack Road, Scott Hall, Columbus, OH 43210, USA.

Email: zou.219@osu.edu

## Funding information

Division of Antarctic Sciences, Grant/Award Numbers: PLR1341695, PLR1443443; Office of Polar Programs, Grant/Award Number: 1823135

## Abstract

The West Antarctic climate is under the combined impact of synoptic and regional drivers. Regional factors have contributed to more frequent surface melting with a similar pattern recently, which accelerates ice loss and favors global sea-level rise. Part I of this research identified and quantified the two leading drivers of Ross Ice Shelf (RIS) melting, viz. foehn effect and direct marine air advection, based on Polar WRF (PWRF) simulations. In this article (Part II), the impact of clouds and the pattern of surface energy balance (SEB) during melting are analyzed, as well as the relationship among these three factors. In general, net shortwave radiation dominates the surface melting with a daily mean value above  $100 \text{ W} \cdot \text{m}^{-2}$ . Foehn clearance and decreasing surface albedo respectively increase the downward shortwave radiation and increase the absorbed shortwave radiation, significantly contributing to surface melting in areas such as western Marie Byrd Land. Also, extensive downward longwave radiation caused by low-level liquid cloud favors the melting expansion over the middle and coastal RIS. With significant moisture transport occurring over more than 40% of the time during the melting period, the impact from net radiation can be amplified. Moreover, frequent foehn cases can enhance the turbulent mixing on the leeside. With a Froude number (Fr) around 1 or slightly larger, fast downdrafts or reversed wind flows can let the warm foehn air penetrate down to the surface with up to  $20 \text{ W} \cdot \text{m}^{-2}$  in sensible heat flux transfer to the ground. However, when the Froude number is close to infinity with breaking waves on the leeside, the contribution of turbulence to the surface warming is reduced. With better understanding of the regional factors for the surface melting, prediction of the future stability of West Antarctic ice shelves can be improved.

## KEYWORDS

clouds, polar WRF, surface energy balance, West Antarctic surface melting

## 1 | INTRODUCTION

The Ross Ice Shelf (RIS) in West Antarctica (WA, Figure 1) has experienced more frequent surface melting in recent

decades, which can result in hydrofracturing of ice shelves and promote ice loss (e.g., Scott *et al.*, 2019). Both synoptic-scale consequences of large-scale drivers (e.g., El Niño) and regional factors, such as foehn effect, direct



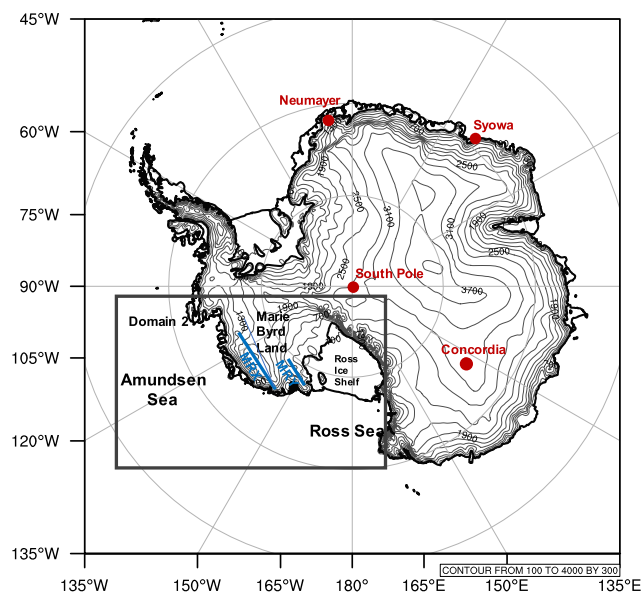


**FIGURE 1** PWRF domains and local topography. Four Baseline Surface Radiation Network stations are marked by red dots. Mountain Range X (MRX) and Mountain Range Y (MRY) are represented by the blue lines. Domain 1 covers a larger area than Figure 1 and is shown in Zou *et al.* (2021) [Colour figure can be viewed at [wileyonlinelibrary.com](http://wileyonlinelibrary.com)]

warm advection, and cloud impacts, have been confirmed to contribute to the surface temperature increase (Nicolas *et al.*, 2017; Scott *et al.*, 2019; Zou *et al.*, 2019). In Part I (Zou *et al.*, 2021), four historical extensive melt cases over the RIS are analyzed based on Polar WRF (PWRF) simulations. Recurring foehn effect, with isentropic drawdown as the dominant factor, occurs during more than 40% of the melting period and contributes an up to 4°C temperature increase, which significantly favors surface melting (Zou *et al.*, 2021). Direct marine air advection from the Ross Sea region mainly affects the coastal RIS adjacent to the Ross Sea and rarely causes impacts farther inland (Zou *et al.*, 2021).

From a surface energy balance (SEB) perspective, latent heat release that is associated with condensation on the upwind side, as a consequence of both marine air advection (or atmospheric rivers) and topographic blocking (foehn), can warm the ice surface on the leeside (Elvidge and Renfrew, 2016; Miltenberger *et al.*, 2016; Bozkurt *et al.*, 2018). Also, turbulent mixing induced by the foehn effect can increase sensible heat flux (SHF) transfer from the upper warm air to the surface (e.g., Steinhoff *et al.*, 2013). In addition, these two factors, viz. direct warm advection and foehn effect, can affect cloud formation and thus have impact on the SEB via downward shortwave/longwave radiation (SWD/LWD); For example, foehn clearance on the leeside can result in abundant SWD via limited cloud (e.g., Cape *et al.*, 2015). In contrast, extra

moisture flux from marine air advection favors cloud formation, which can potentially enhance the LWD (e.g., Nicolas *et al.*, 2017).

Moreover, the impact of clouds on the SEB can be complicated, and the radiative properties of cloud are highly associated with the cloud phase (Gilbert *et al.*, 2020). With large liquid water paths, more longwave radiation will be emitted back to surface due to abundant small droplets (Zhang *et al.*, 1996). Also, cloud can influence the short-wave radiation flux via enhanced scattering, increased condensation, and affecting the spectrum of shortwave radiation reaching the ground (van den Broeke *et al.*, 2006). For instance, mixed-phase clouds with liquid water located at the cloud top are more reflective for shortwave radiation compared with ice cloud, which will decrease the impact of SWD on the SEB (Hogan *et al.*, 2003; Barrett *et al.*, 2017).

The impact of the SEB on surface melting over Antarctica is critical and varies depending on circulation pattern and regional topographic features. Pressure gradients over the topography upstream of the McMurdo Dry Valleys (MDVs) can direct southerly flow into MDVs' western entrance. With complex terrain, the MDVs experience strong mountain waves and, in some cases, foehn events that affect the SEB. Over Taylor Glacier (MDVs), solar radiation (55%) and SHF (40%) primarily contribute to the SEB, while latent heat and longwave radiation are of opposite signs over the entire year (Hoffman *et al.*, 2008). However, during austral summer, the MDVs can have a low value of SHF, which is usually caused by low wind speeds. With clear sky conditions and reduced turbulent fluxes, moderate increase in the total energy reaching the surface can significantly accelerate the melting even with near-surface temperature slightly below the freezing point (Hoffman *et al.*, 2008; Speirs *et al.*, 2013; Steinhoff *et al.*, 2014). The SEB condition is slightly different over the Larsen Ice C Shelf in the Antarctic Peninsula (AP), which has one sharp and narrow mountain range. With prevailing westerly winds, especially under positive Southern Annular Mode, the AP receives increasing warm air advection that can trigger foehn events (Marshall *et al.*, 2006; Cape *et al.*, 2015; Elvidge *et al.*, 2020). Grosvenor *et al.* (2014) suggest that SWD is the most important factor for surface melting because of the clear sky condition caused by foehn events. And the SHF is more likely to be offset by the latent heat loss via sublimation, especially when the foehn jet is warm and dry on the leeside (Grosvenor *et al.*, 2014). Over the RIS, with strong marine air advection from the Amundsen/Ross Sea, the enhanced longwave radiation induced by low-level liquid clouds can prolong the melting (Nicolas *et al.*, 2017). However, under strong foehn cases, the eastern RIS (near Siple Coast) can experience an increase in SWD and SHF, due to foehn clearance and turbulent mixing, respectively (Zou *et al.*, 2019; 2021).



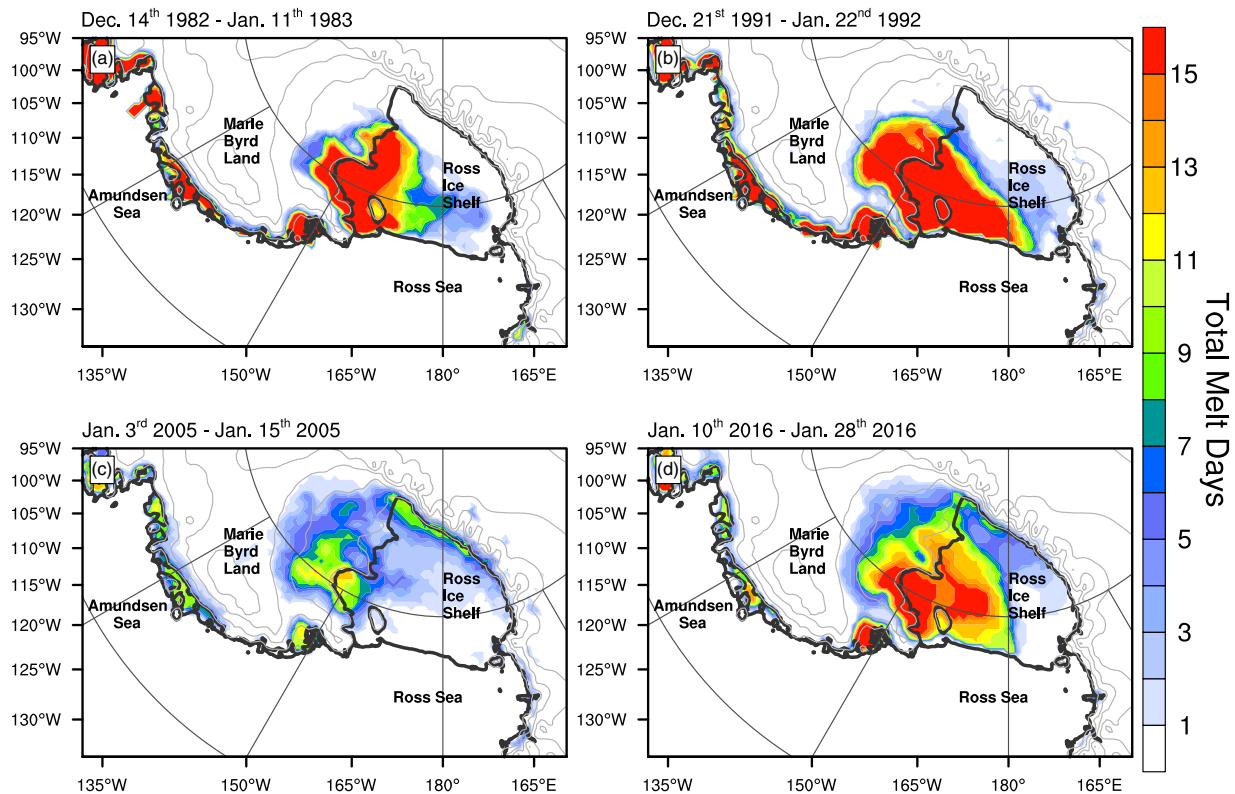


**FIGURE 2** The total melt days of four extensive melt events based on passive microwave satellite observations (data from Nicolas, 2018). The melting period for each case is defined by all days with continuous melting over the RIS during austral summer [Colour figure can be viewed at [wileyonlinelibrary.com](http://wileyonlinelibrary.com)]

To conclude, the SEB pattern can be driven by different mechanisms and has various impacts on surface melting. Correct understanding of these regional factors is critical for the future prediction of ice shelf stability over Antarctica. Previous research mainly investigated the surface melting in the AP and the MDVs, and usually focused on synoptic circulations. This article complements Part I, which identifies and quantifies the contribution of the foehn effect and direct marine air advection on surface melting. Based on four major melt events (Figure 2), this article first demonstrates the SEB condition over the RIS via PWRP simulations, summarizes all potential regional drivers, and then illustrates the relationships among them, which provides a comprehensive explanation for why the melting usually occurs over the RIS during austral summer with a similar pattern.

## 2 | DATA AND METHOD

### 2.1 | Baseline Surface Radiation Network

The Baseline Surface Radiation Network (BSRN) was initiated by the World Climate Research Programme

(WCRP) and provides validation data on the surface radiation budget for climate models (Ohmura *et al.*, 1998; Driemel *et al.*, 2018). Four stations over Antarctica provide high-quality and frequent observations (1 min) of SWD and LWD (Figure 1, Table 1). The high temporal resolution makes BSRN observations a valuable source for radiation scheme validation. Also, regular cleaning of the instruments by permanent staff limits the disruption from riming (Fréville *et al.*, 2014). According to Ohmura *et al.* (1998), the accuracy of LWD measurements is  $2\text{--}3 \text{ W}\cdot\text{m}^{-2}$  based on BSRN standards. BSRN observations have been used in several scientific investigations and can provide reliable estimation of monthly mean values (e.g., Wild, 2008; Roesch *et al.*, 2011). Thus, this study uses hourly BSRN observations to evaluate the model performance of the SEB.

### 2.2 | Moderate Resolution Imaging Spectroradiometer (MODIS) and CERES satellite data

PWRP inputs in this article include surface albedo from MODIS (MCD43C3) for the 2005 and 2016 cases to better simulate the surface conditions (Schaaf and Wang, 2015).



**TABLE 1** Baseline Surface Radiation Network (BSRN) stations

BSRN				
Name	Latitude (°)	Longitude (°)	Elevation (m)	Temporal resolution
Concordia (DOM)	−75.1	123.38	3,233	1 min
Neumayer (GVN)	−70.65	−8.25	42	1 min
South pole (SPO)	−89.98	0	2,835	1 min
Syowa (SYO)	−69.01	39.59	18	1 min

The MODIS albedo with stage 3 validation is produced by the National Aeronautics and Space Administration (NASA) at a 0.05° resolution globally. Previous studies have confirmed the reliability of MODIS albedo, as well as its application in model simulations (e.g., Meng *et al.*, 2018; Song *et al.*, 2019).

Edition 4A (Ed4A) of the Clouds and the Earth's Radiant Energy System (CERES) level 3 daily data includes average computed surface fluxes and satellite-based cloud coverage with 1° horizontal resolution (hereafter referred to as CERES SYN1deg Ed4A) (Loeb *et al.*, 2017). Surface fluxes are calculated based on Terra and Aqua MODIS, geosynchronous satellites (GEO), and assimilated meteorological data (Rutan *et al.*, 2015). CERES SYN1deg Ed4A provides an observation-based dataset to examine the reliability of the SEB and cloud physics in the model output.

### 2.3 | ERA5 reanalysis data and atmospheric rivers detection

This article uses ERA5 reanalysis data to drive PWRF and provides information for the conditions of moisture imports over WA. Produced by the European Centre for Medium-Range Weather Forecasts (ECMWF), ERA5 combines forecast output with archived observations via the data assimilation system. ERA5 provides an hourly global dataset with a ~31 km horizontal resolution and 139 levels in the vertical (Hersbach *et al.*, 2020). Compared with ERA-Interim, ERA5 includes the sources and sinks of all cloud parameters and better represents mixed-phase and supercooled liquid water clouds (Tiedtke, 1993; Silber *et al.*, 2019b). Bozkurt *et al.* (2020) suggest that ERA5 can reduce the warm bias over the Larsen Ice Shelf via a better representation of synoptic forcing. Also, this study investigates the moist imports based on vertical integral of water vapor flux from ERA5, which identifies the source and quantifies the magnitude of the moisture transports. The total flux magnitude is calculated from eastward and northward water vapor fluxes. ERA5, with higher spatial resolution compared with its predecessor, is confirmed to be better at representing atmospheric rivers (ARs) at

Neumayer, East Antarctica (Gorodetskaya *et al.*, 2020). AR detection data produced by Wille *et al.* (2019) from Atmospheric River Tracking Method Intercomparison Project (ARTMIP) tier 1 are also included. It should be noted that ERA5 and CERES SYN1deg Ed4A sometimes have inconsistent information about radiative fluxes and cloud properties, such as the 2016 case (Ghiz *et al.*, 2020). Thus, this article only draws conclusions about cloud impact when ERA5, CERES, MODIS observed albedo, and PWRF provide consistent information on moisture transports, liquid water path, surface melting conditions, and SEB, respectively.

### 2.4 | PWRF model

This article applies PWRF v4.1.1 to simulate the state of atmosphere over Antarctica with a 20-km resolution domain (domain 1) and a 4-km high-resolution nest (domain 2; Figure 1), with 71 vertical levels, the lowest being 4 m above the surface (Zou *et al.*, 2021). As a regional climate model developed by the Polar Meteorology Group of the Byrd Polar and Climate Research Center at The Ohio State University, PWRF can provide reliable near-surface simulations in the polar regions, especially during the austral summer melting (Hines and Bromwich, 2008; Bromwich *et al.*, 2013; Zou *et al.*, 2019). The input data and physical schemes used here are the same as in Part I (Zou *et al.*, 2021). ERA5 reanalysis data provide the initial and lateral boundary conditions, and the PWRF simulations are nudged to ERA5 at stratospheric levels. Morrison 2-moment (Morrison) microphysics scheme, Mellor–Yamada Nakanishi Niino (MYNN) planetary boundary layer scheme, Rapid Radiative Transfer Model for GCMs (RRTMG) radiation scheme, and Unified Noah land surface model are the physics selected to simulate the historical melt events over WA (Nakanishi and Niino, 2004; Morrison *et al.*, 2005; Morcrette *et al.*, 2008). Additionally, for the 2005 and 2016 cases, MODIS observed albedo is included to better describe the changing surface conditions during melting. Developed by the National Center for Atmospheric



Research (NCAR), an Antarctic Mesoscale Prediction System (AMPS, Powers *et al.*, 2012) simulation is used as a benchmark to evaluate the performance of PWRP on the SEB. Both AMPS and PWRP outputs are initialized at 0000 UTC every day and apply a 24-hr model spin-up time.

## 2.5 | Froude number

Figure S1 shows the mountain wave conditions under different values of the Froude (Fr) number, a nondimensional ratio that describes the topographic blocking (Equation 1; Zou *et al.*, 2021).

$$Fr = \frac{U}{NH} \quad (1)$$

where  $H$  is the average effective topographic height,  $N$  is the vertically varying mean-state Brunt–Väisälä frequency below  $H$  (Equation 2), and  $U$  is the vertical varying mean-state wind speed below  $H$ .

$$N = \left( \frac{g}{\theta_0} \frac{\partial \theta_0}{\partial z} \right)^{\frac{1}{2}} \quad (2)$$

where  $g$  is the gravitational acceleration ( $9.81 \text{ m}\cdot\text{s}^{-2}$ ),  $\theta_0(z)$  is the vertically varying mean-state potential temperature, and  $z$  is the height (Durran, 1990).

The Froude number can illustrate the sensible heat transfer between near-surface air and the ground and thus reveal its impact on the SEB. Similar to Zou *et al.* (2021), two groups of Froude numbers are calculated over the mountains over MBL (Figure 1; Mountain Range X, hereafter referred as MRX; effective topographic height of 2,000 m) and Edward VII Peninsula (Mountain Range Y, hereafter referred as MRY; effective topographic height of 800 m), respectively.

## 2.6 | Analysis of surface energy balance and surface melting

The calculation of SEB can be written as Equation 3. When the skin temperature is above the freezing point and SEB is positive, the SEB contributes to the surface melting. Thus, the melt flux is defined as Equation 4 (e.g., King *et al.*, 2017). This article estimates the melt days based on melt flux from PWRP output. When the melt flux over a region is positive for more than 6 hrs per day, this region is counted for the melt day map. All the variables used in Equation 3 to calculate the SEB are from PWRP domain 2 output (4 km).

$$SEB = SW_{\text{net}} + LW_{\text{net}} + LHF + SHF + GFX \quad (3)$$

where  $SW_{\text{net}}$  is the net shortwave radiation,  $LW_{\text{net}}$  is the net longwave radiation, LHF is latent heat flux, SHF is sensible heat flux, and GFX is ground heat flux. All components are positive when they transfer energy to the surface.

$$\text{Melt flux} = \begin{cases} 0, & T_{\text{skin}} < 0^\circ\text{C} \\ SEB, & T_{\text{skin}} \geq 0^\circ\text{C} \end{cases} \quad (4)$$

where  $T_{\text{skin}}$  is the skin temperature (TSK) from PWRP domain 2 output.

## 3 | RESULTS

### 3.1 | Brief model evaluation of surface energy balance

In Part I (Zou *et al.*, 2021), PWRP output driven by ERA5 generates a reliable surface simulation over WA, especially for the temperature field. This article, Part II, provides an additional evaluation on the SEB. Table 2 provides the correlation coefficient ( $R$ ), bias, and root-mean-square error (RMSE) between four BSRN stations and model outputs for downward radiative fluxes. Compared with AMPS, PWRP has a significant improvement in the simulation of surface radiation, in which the average correlation coefficient of shortwave radiation increases from 0.85 to 0.88, the average bias drops from  $43.4$  to  $17.4 \text{ W}\cdot\text{m}^{-2}$  (60.0%), and the average RMSE drops from  $79.0$  to  $66.4 \text{ W}\cdot\text{m}^{-2}$  (15.9%). For LWD, the average  $R$  increases from 0.57 to 0.69, the average bias drops from  $-21.4$  to  $-10.7$  (50.0%), and the average RMSE drops from  $34.1$  to  $27.1 \text{ W}\cdot\text{m}^{-2}$  (20.5%). The improvements in PWRP can result from more advanced physical schemes, better input data from ERA5, and MODIS observed albedo. The bias in SWD and LWD could still be associated with a deficit in cloud liquid water simulated in the model (Hines *et al.*, 2019).

Melt day maps estimated based on daily average melt flux (Figure S2) from PWRP output are shown in Figure 3 (Equations 3 and 4). The strongest surface warming and positive melt flux value were located around Roosevelt Island in the 1982/1983 case, the coastal RIS in the 1991/1992 case, western MBL and the Siple Coast region in the 2005 case, and western MBL area and the whole RIS in the 2016 case. In the 1991/1992 and 2016 cases, the pattern of the cumulative melt day map from PWRP approximates the one that was calculated from passive microwave satellite data, especially for the 2016 case (Figure 2). However, the melting pattern in the 1982/1983 case is not well captured in PWRP. And the melting is overestimated over the center and western RIS in the 2005 case compared with the satellite observations. PWRP output provides hourly melt



**TABLE 2** *R*, bias, and RMSE of downward longwave/shortwave radiation between four Baseline Surface Radiation Network stations and PWRF output for January 2016

AMPS*	Downward shortwave radiation			Longwave downward radiation		
	<i>R</i>	Bias	RMSE	<i>R</i>	Bias	RMSE
Concordia	0.99	14.6	36.9	0.56	−6.4	18.9
Neumayer	0.93	60.9	115.4	0.48	−37.6	52.8
South Pole	0.54	38.3	58.8	0.60	−17.0	27.0
Syowa	0.95	60.1	105.1	0.62	−24.5	37.8
Average	0.85	43.4	79.0	0.57	−21.4	34.1
<b>PWRF_ERA5ALB</b>						
Concordia	0.99	−19.1	36.9	0.70	5.8	17.4
Neumayer	0.95	31.5	91.6	0.70	−20.7	36.0
South Pole	0.64	13.8	43.6	0.71	−10.2	22.7
Syowa	0.95	43.4	93.4	0.66	−17.5	32.3
Average	0.88	17.4	66.4	0.69	−10.7	27.1

\*AMPS has a temporal resolution of 3 hr, and PWRF output has a temporal resolution of 1 hr. South Pole does not have a diurnal cycle in the downward shortwave radiation resulting in a lower correlation coefficient (*R*). PWRF\_ERA5ALB represents the PWRF simulations driven by ERA5 reanalysis data and MODIS observed albedo.

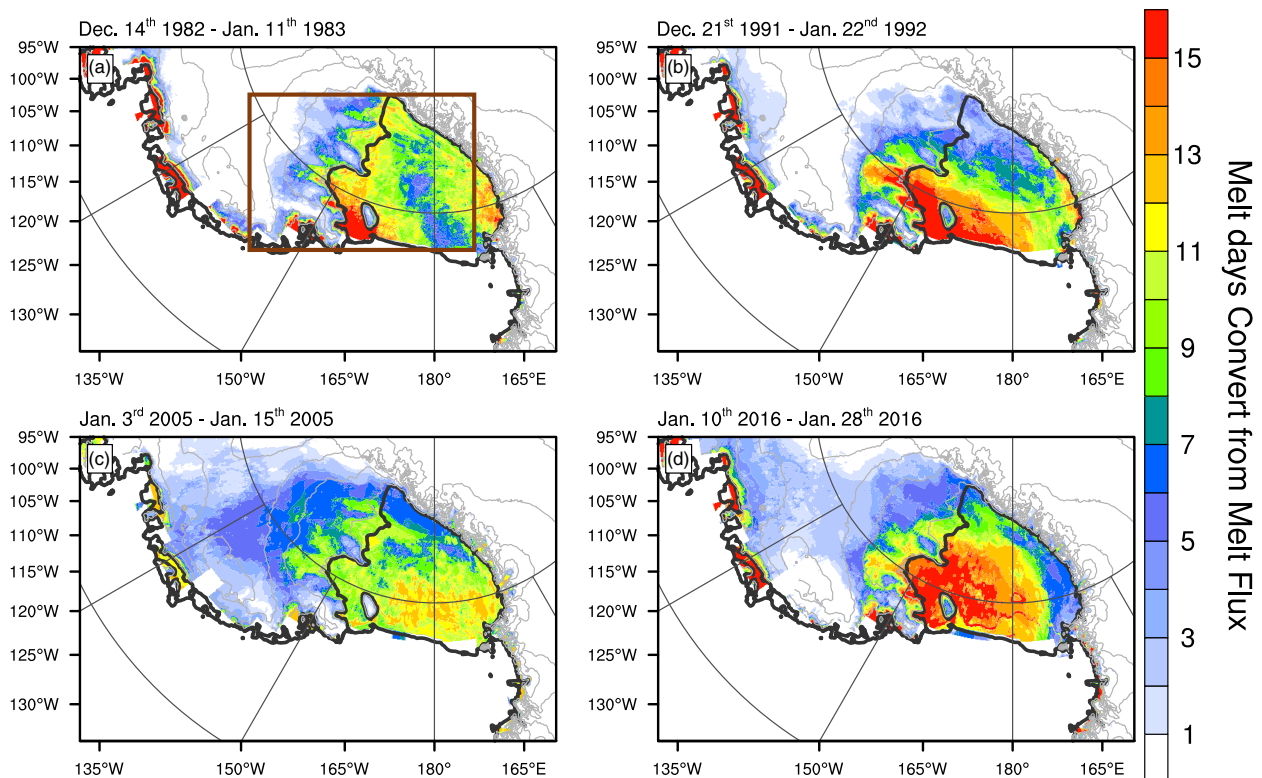


**FIGURE 3** The melt days calculated based on surface melt flux for four historical melt events based PWRF domain 2 outputs. Variables from PWRF used in the calculation are as follows: downward shortwave radiation (SWD), upward shortwave radiation (SWU), downward longwave radiation (LWD), upward longwave radiation (LWU), sensible heat flux (SFX), latent heat flux (LH), and ground heat flux (GFX). Brown box in (a) represents the area used to calculate the time series of surface energy balance in Figure 4 [Colour figure can be viewed at [wileyonlinelibrary.com](http://wileyonlinelibrary.com)]



flux spatial maps, and only regions with positive melt flux for more than 6 hrs per day are counted as a melt day. In contrast, the satellite-based melt day is estimated based on twice-daily observations of brightness temperature, which can result in different melt days compared with the model output. Furthermore, for the 2012–2017 period, corrections have been applied to the Terra MODIS (Reflective Solar Bands).<sup>1</sup> Thus, in the 2016 case, the consistency of the pattern between PWRP output and satellite data is the best (Figure S2), which can result from the higher-quality MODIS observed albedo introduced into the model simulation (Figure S3). Another difference in melt day pattern between these two sources occurs along the Transantarctic Mountains, where PWRP output shows moderate melting (e.g., 1982/1983 and 1991/1992). This could be associated with the katabatic winds from the East Antarctic plateau via Byrd Glacier near 80° S that are anomalously dry due to omission of the blowing snow processes in PWRP (Wille *et al.*, 2016); further investigation is necessary.

Modeled clouds are critical for the simulation of surface conditions, such as the surface energy balance. The advanced Morrison microphysics scheme (cloud related) used in the PWRP runs contributes the most to the improved simulation of downward surface radiation. For high-resolution models, the Morrison scheme is able to resolve the maximum supersaturation and simulate supercooled liquid water, which is critical for liquid cloud formation (e.g., Morrison *et al.*, 2009; Hines *et al.*, 2019). In the Listowski and Lachlan-Cope (2017) cloud simulation over the AP, the Morrison scheme had the best agreement with the observations in occurrence and phase. Correct simulation of the liquid clouds is critical for accurate simulation of LWD. In general, based on the comparison between observations and model outputs, the PWRP can provide a reliable simulation of the net radiative fluxes.

### 3.2 | Overview of the surface energy balance over West Antarctica

To demonstrate the contribution of each component ( $SW_{net}$ ,  $LW_{net}$ , SHF, LHF, and GFX) in the SEB to surface melting (Equation 3), Figure 4 illustrates their daily change for all cases over WA (inside brown box in Figure 3a), as well as the melt flux. Zou *et al.* (2021) suggested that all cases except the 2005 one have multiple melting periods with differing dominant mechanisms during the event, which is confirmed by the daily melt flux. The 1982/1983, 1991/1992, and 2016 cases show an increase in melt flux around 12 days after the start of the

event, especially for the 1991/1992 and 2016 cases. At the beginning of the melt case, the direct warm air advection plays an important role. With the shift in regional circulation pattern, stronger foehn effect can result in a surface melting expansion (e.g., 2016 case, Figure S4).

During the whole event for all melt cases,  $SW_{net}/LW_{net}$ , with a daily mean value over  $100 \text{ W}\cdot\text{m}^{-2}$ /less than  $-20 \text{ W}\cdot\text{m}^{-2}$ , usually dominates the SEB over western MBL and the RIS compared with SHF and LHF, with values up to 10 times smaller. In the 1982/1983, 1991/1992, and 2005 cases,  $LW_{net}$  is almost constant during the melting. In contrast, the 2016 case experiences a more negative  $LW_{net}$  with time, which is associated with its widespread and intensified melting that contributes to the increased upward long-wave radiation (LWU). Also, all cases show an increase in  $SW_{net}$ , especially for the 2016 case ( $\sim 100 \text{ W}\cdot\text{m}^{-2}$ ), which results from increasing SWD caused by foehn clearance and decreasing upward shortwave radiation (SWU) caused by lower surface albedo (after 21 January). Additionally, the contribution of SHF in the 2005 and 2016 cases is mainly limited to the leeside of MRX and MRY, thus it only demonstrates a less than  $10 \text{ W}\cdot\text{m}^{-2}$  contribution to the daily average SEB at the beginning of the events. The contribution of LHF is negative for all four cases due to the melting surface, and the impact of GFX is small in this study. The following sections discuss the contribution of each component in detail, as well as the formation conditions.

### 3.3 | Cloud impacts on $SW_{net}$ and $LW_{net}$

This section analyzes the surface net radiation and investigates the cloud conditions during melt events, especially for periods of melt area expansion. The analysis is based on PWRP domain 2 output (spatial resolution 4 km), ERA5 reanalysis data, and CERES and MODIS satellite observations. Because CERES and MODIS start from 2002, the cloud conditions in the 1982/1983 and 1991/1992 cases are analyzed mainly based on ERA5 reanalysis data.

The formation of clouds plays an important role in surface energy balance over Antarctica and is highly associated with the moisture import from the surrounding ocean. With a liquid water path value between 10 and  $40 \text{ g}\cdot\text{m}^{-2}$ , liquid clouds can allow adequate short-wave radiation through to the surface and also generate enough LWD (Bennartz *et al.*, 2013). Figure 5 shows the hourly integrated water vapor transport (IVT) from ERA5 reanalysis data, and Table 3 summarizes the days with strong moisture imports for each melt case. The 2005 and 2016 cases have more powerful moisture transport ( $\sim 100 \text{ kg}\cdot\text{m}^{-1}\cdot\text{s}^{-1}$ ) from the Amundsen/Ross Sea region toward coastal WA, which can be an explanation for their

<sup>1</sup> [https://cmr.earthdata.nasa.gov/search/concepts/C1620282523-LPDAAAC\\_ECS.html](https://cmr.earthdata.nasa.gov/search/concepts/C1620282523-LPDAAAC_ECS.html)



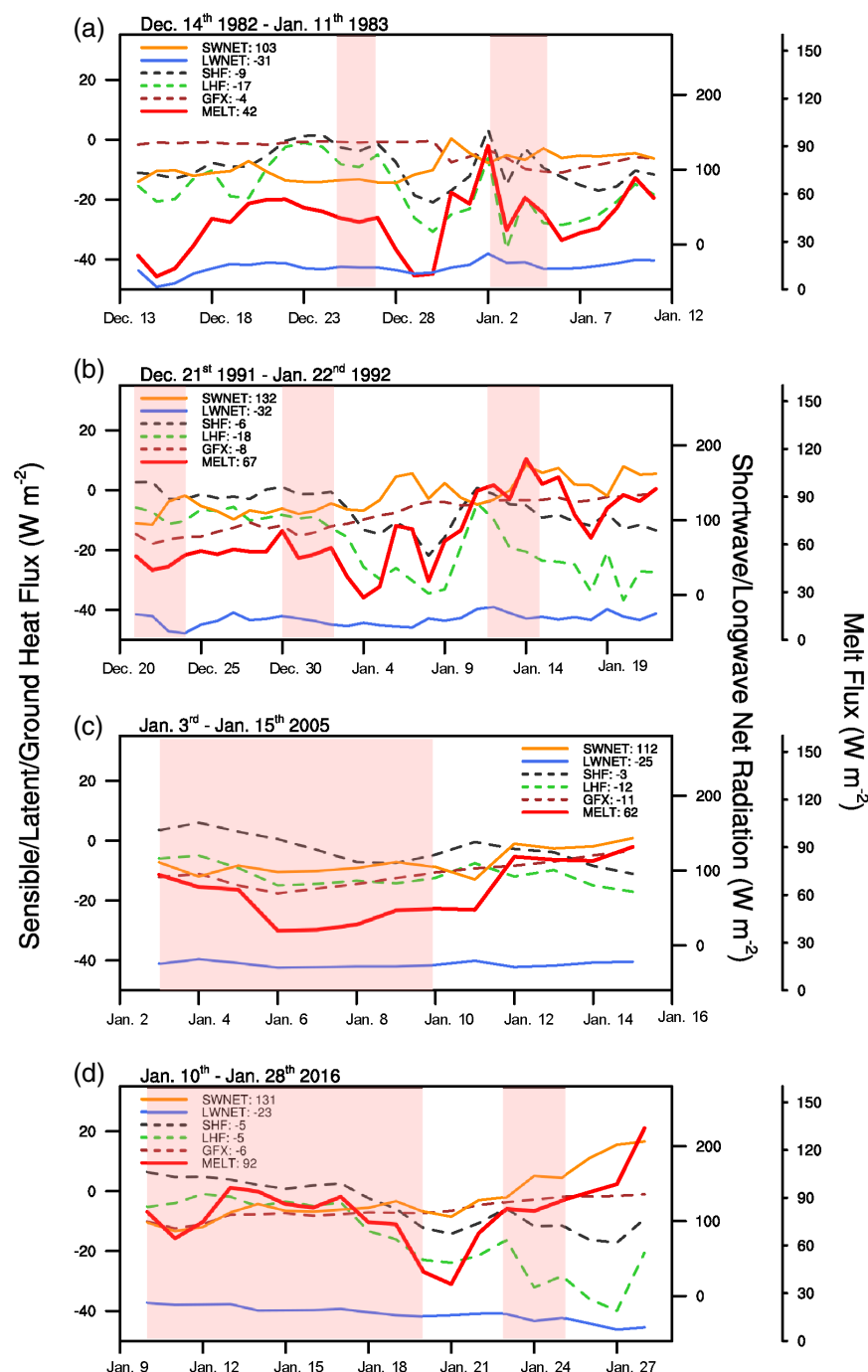


**FIGURE 4** Time series of daily average longwave/shortwave net radiation (SWnet /LWnet), sensible heat flux (SHF), latent heat flux (LHF), ground heat flux (GFX), and melt flux (MELT) over western Marie Byrd Land and Ross Ice Shelf (inside the brown box in Figure 3a). Left Y axis is for SHF, LHF, and GFX (dashed lines), the right Y axis closer to the panel is for SWnet and LWnet, and the right Y axis away from the panel is for melt flux. The contribution of each component is calculated when surface melting occurs. The numbers in the legend represent the average of each component during the melting period. The pink shadow represents the foehn events [Colour figure can be viewed at [wileyonlinelibrary.com](http://wileyonlinelibrary.com)]

similar melting patterns, short duration, and intensified melting. The 2005 and 2016 cases expand further inland toward the Transantarctic Mountains and western MBL in a short time period. In contrast, the 1982/1983 case lacks direct moisture transport toward coastal MBL but more toward the eastern RIS ( $\sim 20 \text{ kg} \cdot \text{m}^{-1} \cdot \text{s}^{-1}$ ), and the 1991/1992 case mainly has moderate water vapor imports ( $\sim 40 \text{ kg} \cdot \text{m}^{-1} \cdot \text{s}^{-1}$ ) toward the coastal RIS. This direct warm marine advection leads to prolonged and slower spread melt events in 1991/1992 and 1982/1983 (Zou *et al.*, 2021). Furthermore, less moisture flux can indicate less significant cloud impact on LWD.

With different regional circulation patterns and moisture imports, the RIS can experience various cloud impacts on the SEB, and thus affect the surface melting. To demonstrate the detailed contribution of clouds, two representative days in the 2016 case are selected for further exploration, which illustrates the contrast between two different phases. The average liquid water path anomaly from CERES, cross-section of mixing ratio and previous 12-hr precipitation accumulation based on PWRP output on January 10, 2016, and IVT from ERA5 reanalysis data are shown in Figure 6. At the beginning of the 2016 case (10 January), strong moisture transport was directed at the



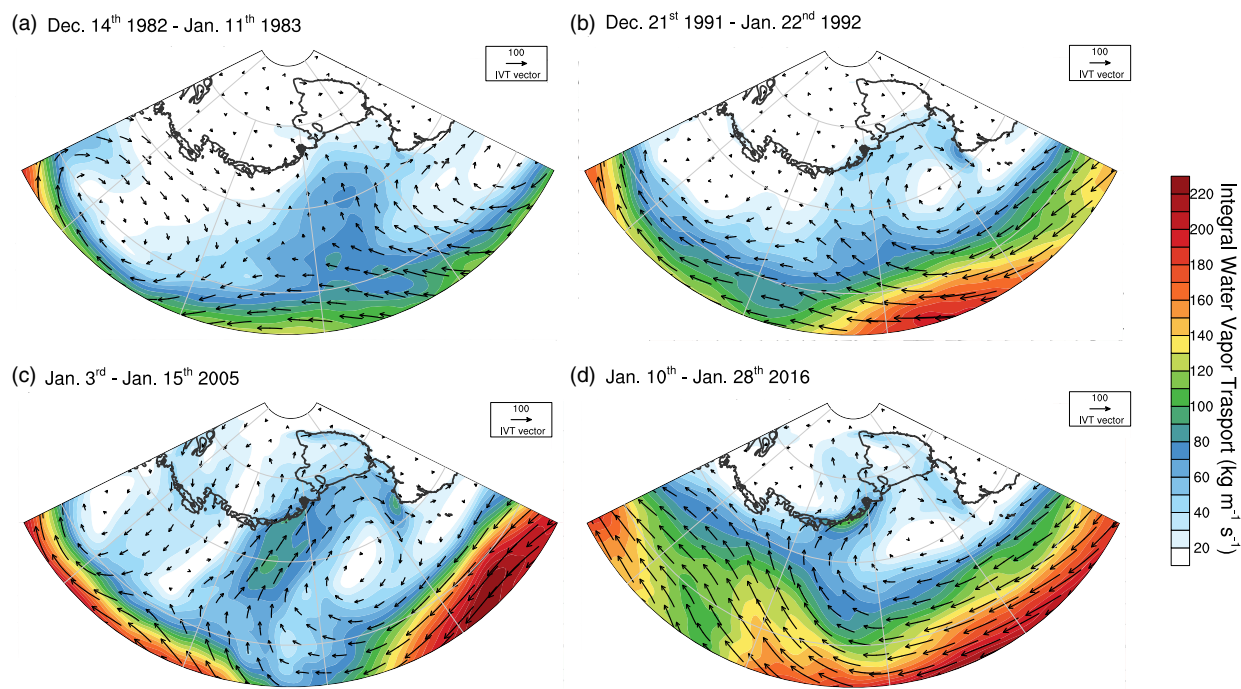


**FIGURE 5** Spatial distribution of hourly integrated water vapor transport (IVT) for the four melt cases over West Antarctica from ERA5 reanalysis data. The ERA5 IVT is the composite of integral of northward and eastward water vapor flux, which is calculated from the Earth's surface (1,000 hPa) to model top (1 hPa) [Colour figure can be viewed at [wileyonlinelibrary.com](http://wileyonlinelibrary.com)]

**TABLE 3** Days having moisture input from the ocean during the melting period (underlines mark abundant moisture flux)

Moisture flux (based on ERA5 reanalysis data)				
Year	1982/83	1991/92	2005	2016
Days with moisture flux from ocean (%)	12 (41%)	11 (33%)	5 (39%)	12 (63%)
Days with strong Moisture flux	4	0	5	9
Detailed dates	December 14–16 December 28–29 <u>January 2–5</u> January 8–10	December 21–26 December 29–January 2	<u>January 3–7</u>	January 10–18 January 23–25
ARs detection (Wille <i>et al.</i> , 2019)				
Days with ARs	N/A	December 23–24	January 4 and 6	January 10–13

Sulzberger Ice Shelf ( $\sim 150^\circ$  W, Figure 5d), which led to intense precipitation on the upwind side of MRY and abundant water vapor blowing into the coast of the eastern RIS (Figure 6c). Thus, the leeside of MRY has a mixing ratio of over  $3 \text{ kg} \cdot \text{g}^{-1}$  from the surface to 2 km altitude (Figure 6b). Under this circumstance, low-level liquid clouds are easily formed and play a significant role in the SEB (Figure 6a). Figure 7 shows hourly average SWD, LWD, SHF, and LHF over the RIS on 10 January from PWRP output. Consistent with the liquid cloud pattern from CERES, the coastal

eastern RIS experiences a less than  $250 \text{ W} \cdot \text{m}^{-2}$  SWD and more than  $300 \text{ W} \cdot \text{m}^{-2}$  LWD. SHF and LHF have a smaller impact on SEB compared with surface net radiation. However, on the leeside of MRY, a downward SHF exceeding  $20 \text{ W} \cdot \text{m}^{-2}$  caused by turbulent mixing favors the start of the melting.

During the peak of the 2016 case (18 January, Figure 8), moderate moisture intrusion occurred (from the Amundsen Sea) along coastal MBL ( $110\text{--}150^\circ$  W, Figure 8d). Due to the condensation on the upwind side (coastal MBL)



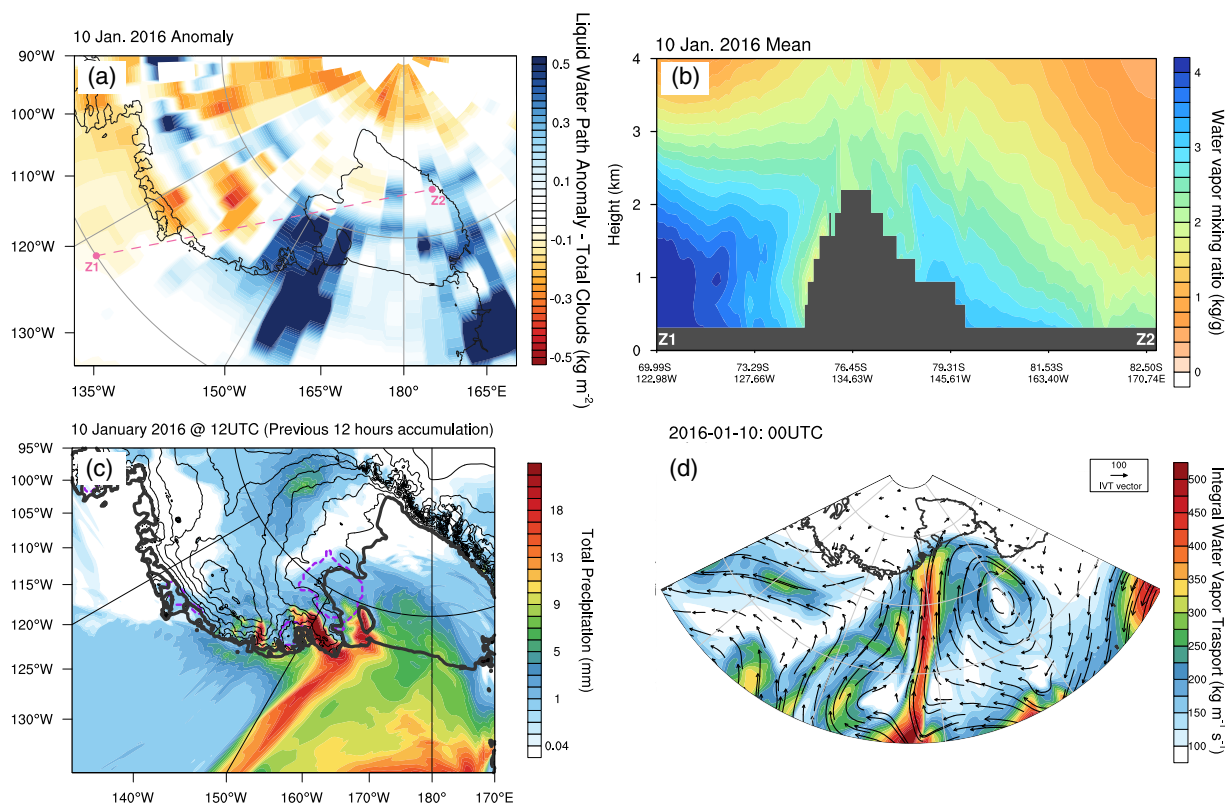


**FIGURE 6** (a) Liquid water path anomaly from CERES on the January 10, 2016 based on the monthly mean; (b) vertical profiles of average mixing ratio from PWRF domain 2 output on January 10, 2016, (c) prior 12-hr precipitation accumulation from PWRF domain 2 output on January 10, 2016 at 1200 UTC, and (d) spatial distribution of integrated water vapor transport on January 10, 2016 at 0000 UTC from ERA5 reanalysis data. Dashed purple lines in (c) represent daily melting area. The base for the anomaly is January 2–30, 2016 [Colour figure can be viewed at [wileyonlinelibrary.com](http://wileyonlinelibrary.com)]

caused by orographic lifting (Figure 8c), the leeside of the MRX (western MBL and Siple Coast region) experiences strong foehn clearance. Both CERES liquid water path anomaly and cross section of mixing ratio (less than  $1.5 \text{ g} \cdot \text{kg}^{-1}$  near the surface) based on PWRF show relatively dry and clear sky conditions over the Siple Coast region. Limited liquid cloud introduces extensive SWD over inland area of the eastern RIS with an hourly average of over  $400 \text{ W} \cdot \text{m}^{-2}$ , and the LWD decreases to  $200 \text{ W} \cdot \text{m}^{-2}$  (Figure 9). In addition, weak precipitation was simulated along the coast of the middle RIS, and the source of moisture can come from the Ross Sea and sublimation from the melting surface, which explains the  $\sim 300 \text{ W} \cdot \text{m}^{-2}$  LWD. Nicolas *et al.* (2017) suggest that the low-level liquid cloud contributed to surface melting expansion in the middle RIS via extensive LWD radiation. And Hu *et al.* (2019) claim that a deep warm air column between 800 and 500 hPa also increases the LWD, which accounts for 60% of the increase in LWD. Similar to 10 January, SHF and LHF have less impact on SEB compared with SWD and LWD. The second phase (18 January) favors the westward expansion of

the RIS melting in the 2016 case and is also the dominant phase in the 2005 case (Figures S5 and S6).

Figure 10 shows the average cloud cover at different heights for the 2005 and 2016 cases from CERES. With strong moisture imports, both cases have more than 80% total cloud fraction during the melt period, especially for low-level clouds over the middle RIS. The clear sky conditions over western MBL and Siple Coast did not last for the whole melt period in the 2005 case, thus this pattern is vague in the average cloud fraction. Based on the analysis for 2005 and 2016 cases, the coastal RIS and middle RIS tend to have stronger LWD caused by low-level liquid clouds, and the eastern RIS and western MBL (around Siple Coast region) are more likely dominated by the SWD caused by foehn clearance. The continuous increase in  $\text{SW}_{\text{net}}$  in Figure 4, especially for the 2016 case, confirms the combined contribution of both increasing SWD and decreasing SWU. The increasing LWD results from low-level liquid clouds, but this can be compensated by the LWU increase caused by surface melting, and lead to a neutral or negative  $\text{LW}_{\text{net}}$ . Thus,  $\text{SW}_{\text{net}}$  in general plays



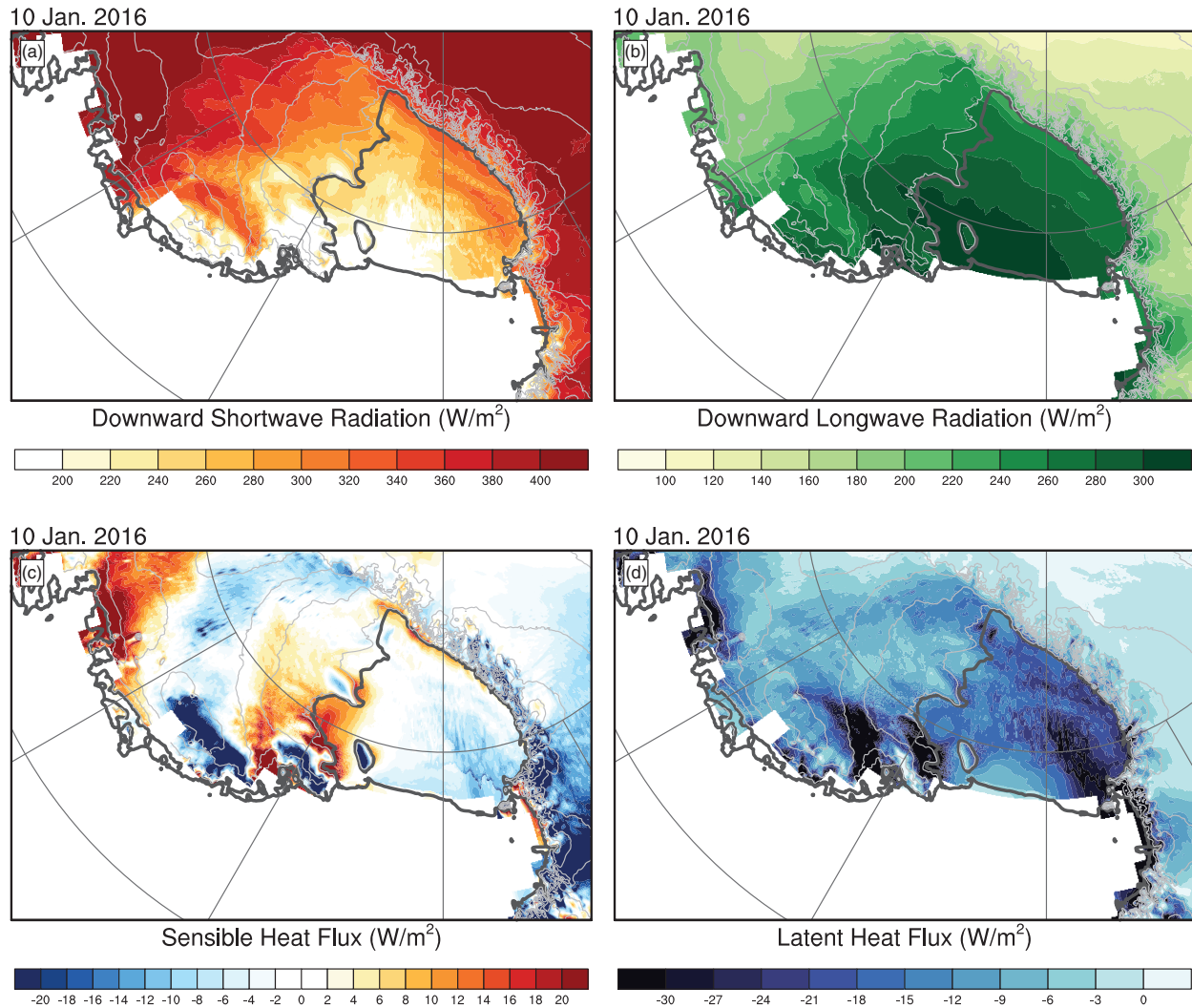


**FIGURE 7** Daily average of hourly average downward shortwave radiation, downward longwave radiation, sensible heat flux, and latent heat flux on January 10, 2016 from PWRP domain 2 outputs. Negative sign represents upward energy transfer, and positive represents downward energy transfer [Colour figure can be viewed at [wileyonlinelibrary.com](http://wileyonlinelibrary.com)]

a more important role compared with  $LW_{net}$  over the West Antarctic continent.

Figure 11 shows the hourly average surface LWD and SWD anomaly for all four melt cases from PWRP domain 2 output, which are consistent with the IVT from the ERA5 reanalysis data and the liquid water path from CERES data (only for the 2005 and 2016 cases). In the 1982/1983 case, the eastern RIS surface melting is dominated by extensive LWD with an anomaly of  $\sim 80 \text{ W} \cdot \text{m}^{-2}$ , which compensates the slight cooling impact from the deficit in SWD ( $\sim 16 \text{ W} \cdot \text{m}^{-2}$ ). In the 1991/1992 case, an up to  $48 \text{ W} \cdot \text{m}^{-2}$  anomaly in LWD contributes to the coastal melting over the RIS, with a  $\sim 16 \text{ W} \cdot \text{m}^{-2}$  deficit in the SWD anomaly. In the first two melt cases, weaker moisture transport toward MBL and foehn effect are observed (Zou *et al.*, 2021), which results in less SWD increase associated with foehn clearance and more direct warming from marine air. Thus, the

$SW_{net}$  increases steadily and  $LW_{net}$  is almost constant for the 1982/1983 and 1991/1992 cases (Figure 4). This favors a prolonged and moderate melting over the RIS and is limited to the coastal area. In the 2005 case, strong moisture flux toward MBL leads to a positive anomaly in SWD ( $\sim 48 \text{ W} \cdot \text{m}^{-2}$ ) around western MBL and the Siple Coast region, which contributes to the start of the melting. However, moisture imports weakened on 6 January and ceased after 8 January, thus the contribution of SWD did not last for the 2005 case, which leads to a moderate increase in  $SW_{net}$  with time (Figure 4). Also, an up-to  $80 \text{ W} \cdot \text{m}^{-2}$  positive anomaly in LWD over the western RIS reveals the moisture import from the Ross Sea and potential sublimation near the surface, which accelerates the expansion of the melting. At the beginning of the 2016 case (10 January), Nicolas *et al.* (2017) suggested that the eastern RIS had an increase in LWD over the Siple Coast region



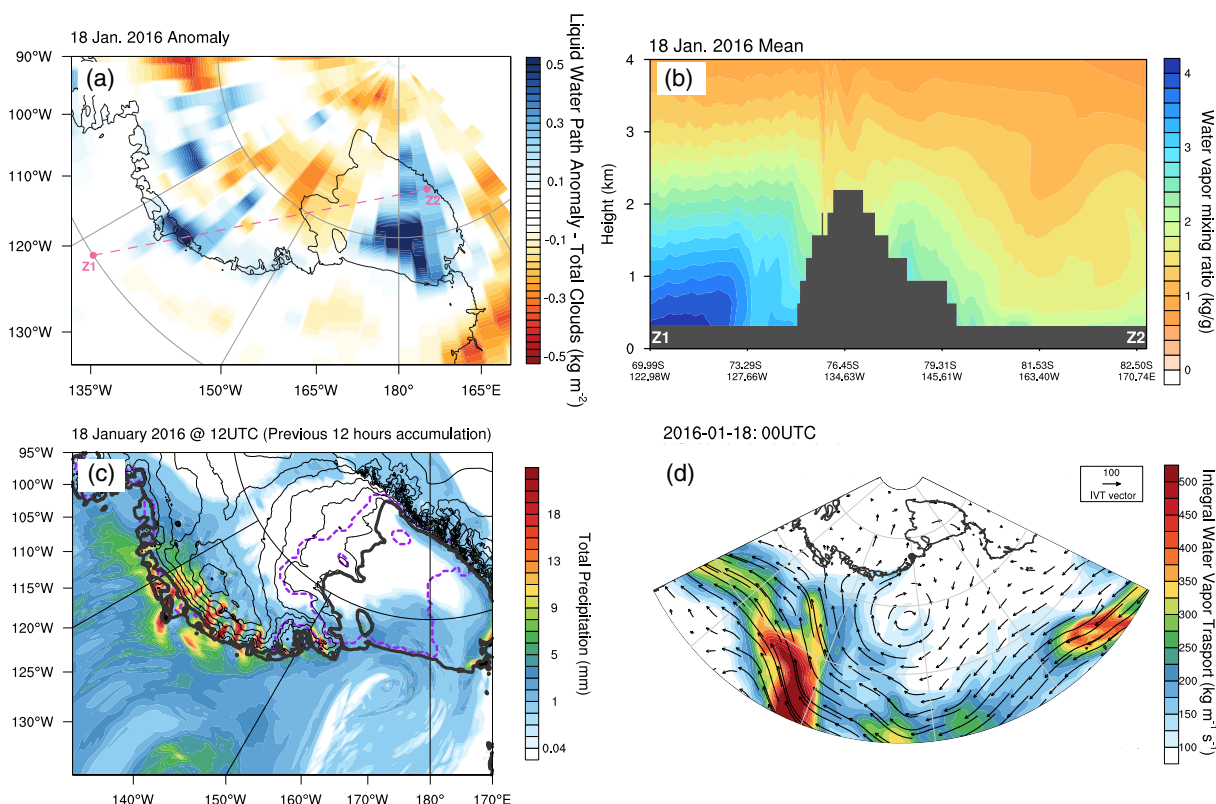


**FIGURE 8** (a) Liquid water path anomaly from CERES on January 18, 2016 based on the monthly mean; (b) vertical profiles of average mixing ratio from PWRP domain 2 output on January 18, 2016, (c) prior 12-hr precipitation accumulation from PWRP domain 2 output on January 18, 2016 at 1200 UTC, and (d) spatial distribution of integrated water vapor transport (IVT) on January 18, 2016 at 0000 UTC from ERA5 reanalysis data. Dashed purple lines in (c) represent daily melting area. The base for the anomaly is January 2–30, 2016 [Colour figure can be viewed at [wileyonlinelibrary.com](http://wileyonlinelibrary.com)]

due to direct warm advection from Ross Sea. As the surface melting has developed, the foehn effect plays a more important role and increases the SWD over the Siple Coast (e.g., 18 January). The significant increase in  $SW_{net}$  is partially caused by the SWD (Figure 4). However, during the whole 2016 case, the LWD anomaly over the middle RIS is around  $20 \text{ W} \cdot \text{m}^{-2}$  and the SWD anomaly is negative, which indicates LWD contributes more to the expansion of the melting (Figures 11g,h). The extensive melting results in a LWU increase and offsets the LWD, which finally leads to a more negative  $LW_{net}$  (Figure 4).

### 3.4 | SHF and mountain waves

Besides the  $SW_{net}$  and  $LW_{net}$  that are affected by the cloud conditions, SHF is another important component in the SEB over the eastern RIS and is usually associated with mountain waves. Figure 12 shows the cross-section of hourly average turbulent kinetic energy, describing the magnitude of the turbulence for the representative days of each melt event. Over MRY, turbulent kinetic energy

is usually larger than over MRX, which is consistent with the larger Froude numbers that have been calculated over MRY. For the representative day, both the 1982/1983 and 2016 cases have strong turbulence and sensible heat transfer that occurred on the leeside of MRX and MRY, which indicates that turbulence can contribute to the energy transfer to the surface.

Figures 13 and 14 show the distribution of daily Froude number and hourly average SHF for the four melt cases based on PWRP domain 2 output, respectively. SHF is a significant contributor to the surface melting for certain areas (e.g., western MBL), especially for the 2016 case. The time series of SHF in Figure 4 also suggest that the 2005 and 2016 cases experience slightly more influence from turbulent mixing compared with the other two cases. When warm and moist air crosses the higher mountain range over MBL (MRX), strong turbulence occurs on the leeside and brings warmth to the surface of western MBL. In the 2016 case, the average Fr over MRX is  $\sim 0.39$ , which is the highest compared with all other cases (1982/1983: 0.29; 1991/1992: 0.27; 2005: 0.30). Over MRX, the daily Froude number in 1982/1983 and 1991/1992 cases mainly range



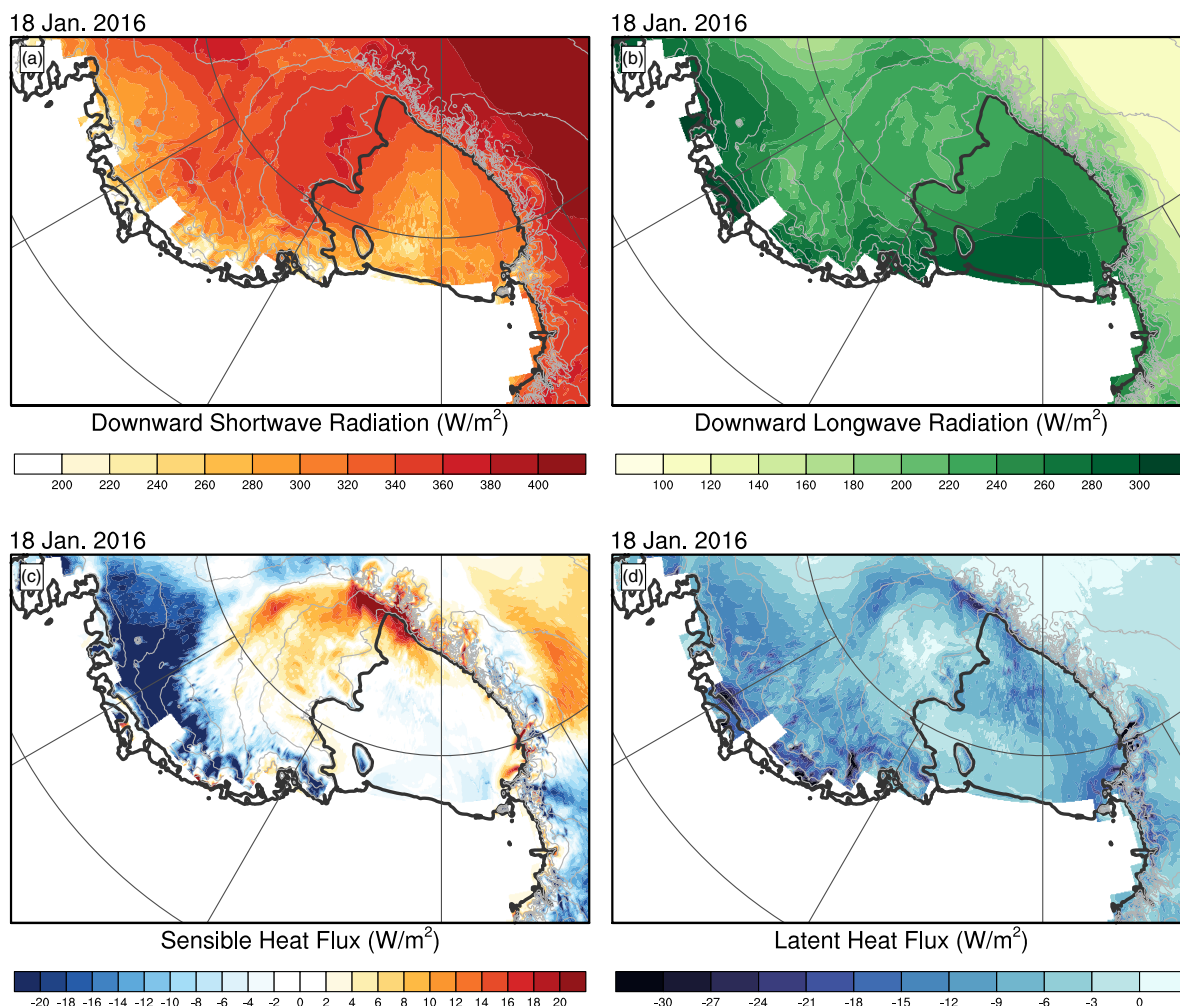


**FIGURE 9** Daily average of hourly average downward shortwave radiation, downward longwave radiation, sensible heat flux, and latent heat flux on January 18, 2016 from PWRF domain 2 outputs. Negative sign represents upward energy transfer, and positive represents downward energy transfer [Colour figure can be viewed at [wileyonlinelibrary.com](http://wileyonlinelibrary.com)]

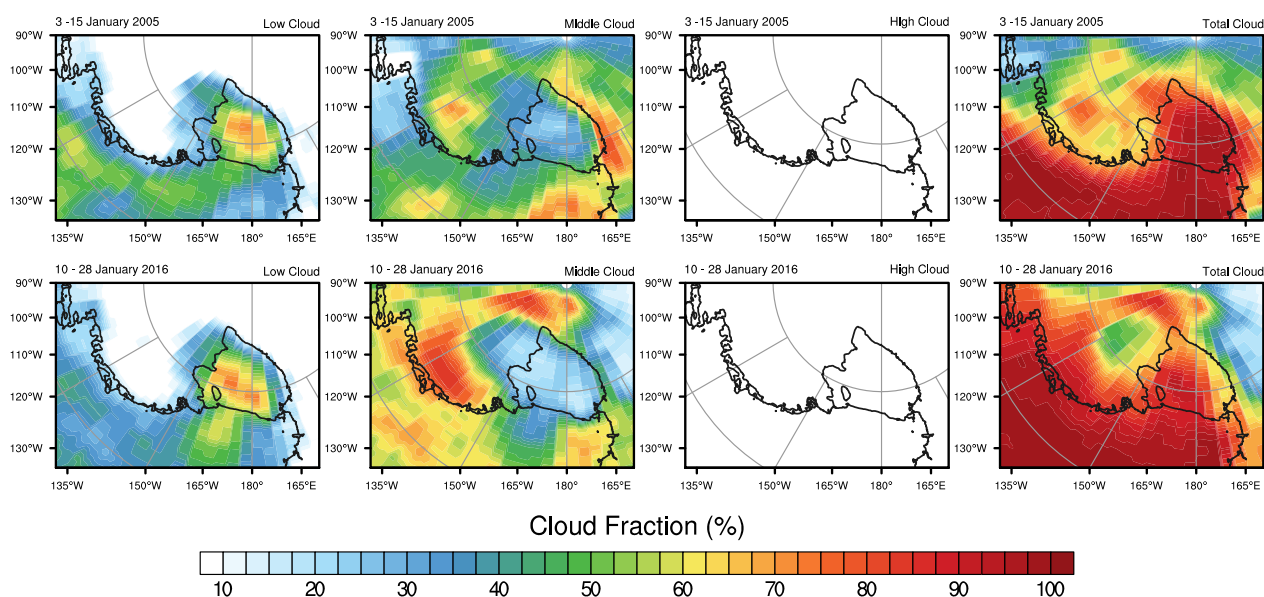


**FIGURE 10** Average CERES cloud fraction data during 2005 and 2016 melt cases. (low cloud: surface – 700 hPa; middle cloud: 700–300 hPa; high cloud: 300 hPa – tropopause) [Colour figure can be viewed at [wileyonlinelibrary.com](http://wileyonlinelibrary.com)]



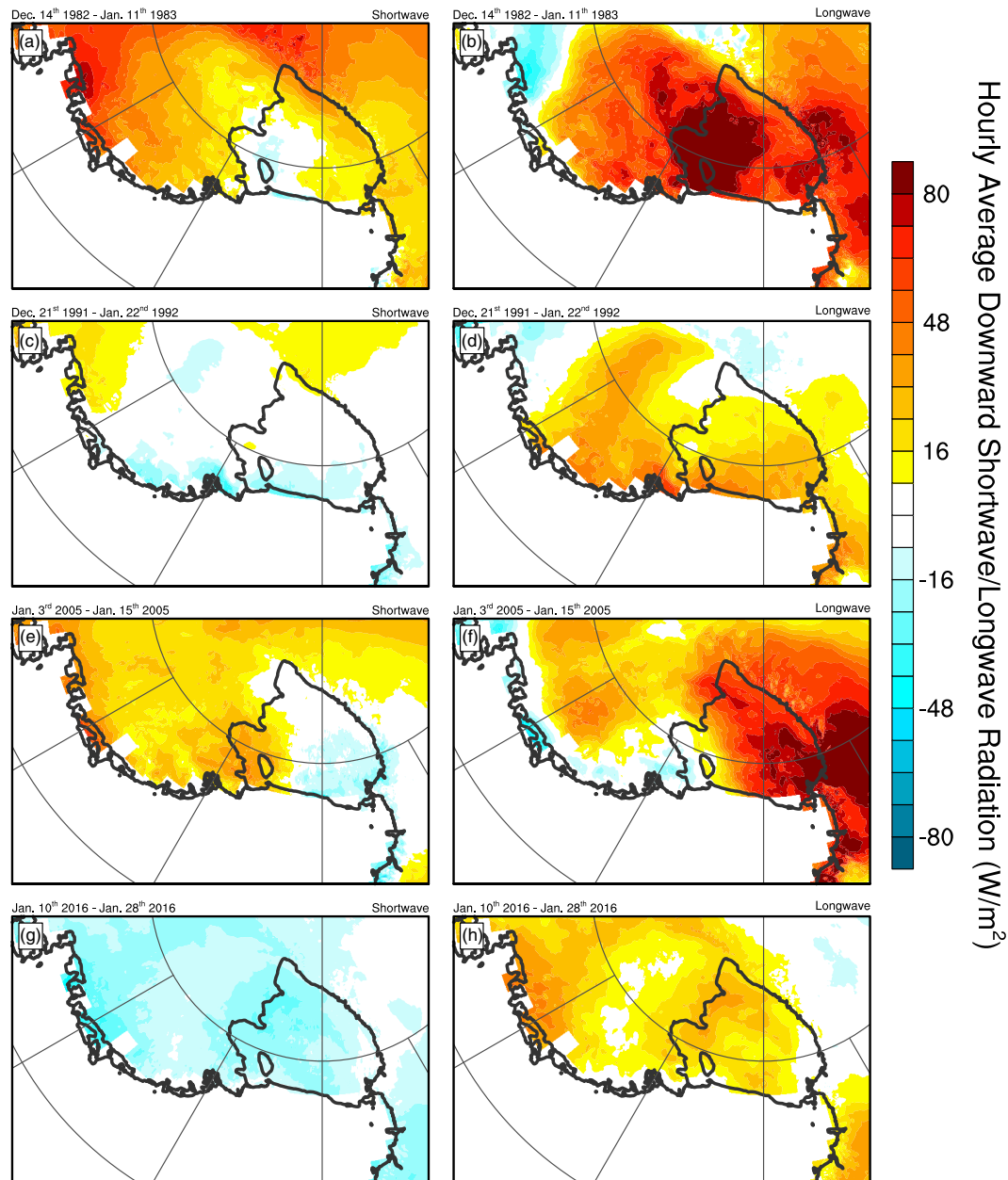


**FIGURE 11** Hourly downward shortwave and longwave radiation anomaly for the four melt cases based on PWRP domain 2 outputs. The baseline for the 1982/1983 case is December 1982 and January 1983, the baseline for the 1991/1992 case is December 1991 and January 1992, the baseline for the 2005 case is January 2005, and the baseline for the 2016 case is January 2016 [Colour figure can be viewed at [wileyonlinelibrary.com](http://wileyonlinelibrary.com)]

between 0 and 0.3, while in 2005 and 2016 cases, the number is usually larger than 0.3 (46.3 and 83.9%, respectively). This leads to a significant difference in sensible heat transfer between the first two melt cases (1982/1983 and 1991/1992 cases) and the latter two (2005 and 2016 cases), which has a stronger positive impact, especially the 2016 case (inside the red boxes in Figures 13 and 14). Even with more violent mountain waves, the contribution of sensible flux over MRY is not as strong as over MRX. The 2005 and 2016 cases have more days with a Froude number

between 0 and 40 than a Froude number above 100, and the 1982/1983 and 1991/1992 cases have slightly more days with a Froude number larger than 40 ( $\sim 34\%$ ) compared with the other cases (Figure 13). The distribution of daily Froude number indicates that the SHF is more likely to have a positive impact over WA when the Froude number is between 0.3 and 40. Briefly, when the Froude number is  $\sim 1$  or  $>1$  (but not approaching infinity), more violent and faster downdrafts will be found on the leeside, such as cavities. Thus, the enhanced sensible heat transfer between



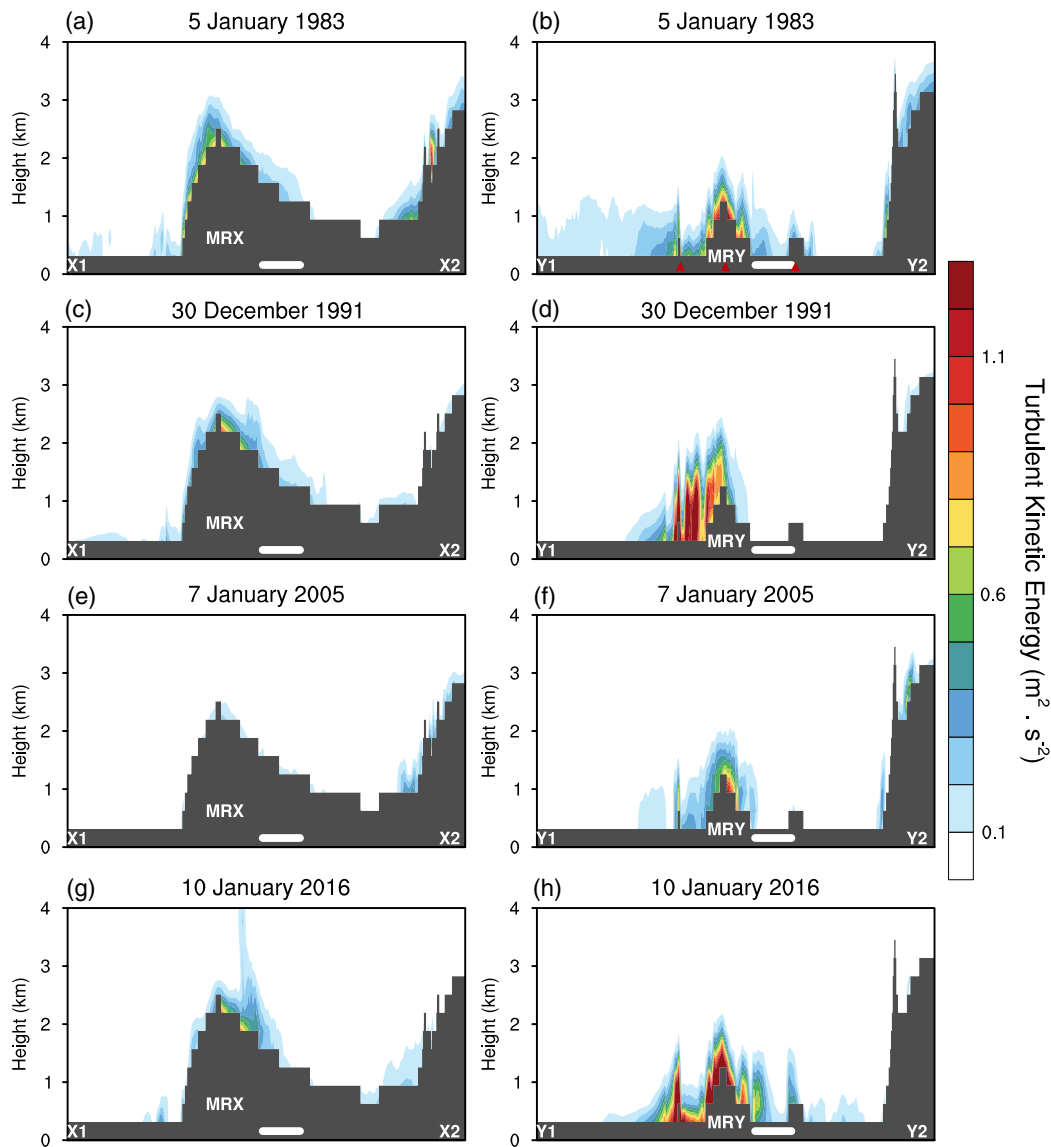


**FIGURE 12** Hourly average turbulent kinetic energy on representative day for each melt case. White solid line represents the approximate location of the melting area. Over the cross-section for MRY, there are three topographic barriers along the path (red triangles in Figure 12b) [Colour figure can be viewed at [wileyonlinelibrary.com](http://wileyonlinelibrary.com)]

foehn flow and surface air will amplify the melting. However, the contribution of SHF is mainly limited to western MBL region and is much smaller compared with surface net radiation (Figure 4).

## 4 | DISCUSSION

The ARs, narrow corridors of intense moisture transport, can significantly impact the surface mass balance via enhanced snowfall or increased melt energy in polar regions (e.g., Mattingly *et al.*, 2018). Wille *et al.* (2019) suggest that ARs could be responsible for  $\sim 40\%$  of the summer melting over the RIS and nearly 100% over MBL

at higher elevations. In this article, we confirm the significant contribution of strong moisture imports from the Amundsen/Ross Sea to the surface warming over WA. The magnitude of the contribution, however, requires further evaluation. Based on the IVT from ERA5 for all four melt cases, more than 30% of the time on average has strong moisture transport toward the eastern RIS or the coast of WA (Figure 5, Table 3). The 1982/1983 case has moisture transport from the ocean ( $\sim 41\%$ ), which is directed toward the eastern RIS and the Sulzberger Ice Shelf (December 14–18) and then shifts to the coast of MBL (January 2–5). The 1991/1992 case intermittently has a weaker moisture transport and mainly toward the Sulzberger Ice Shelf and the RIS ( $\sim 33\%$ ). In contrast, the 2005 and 2016 cases



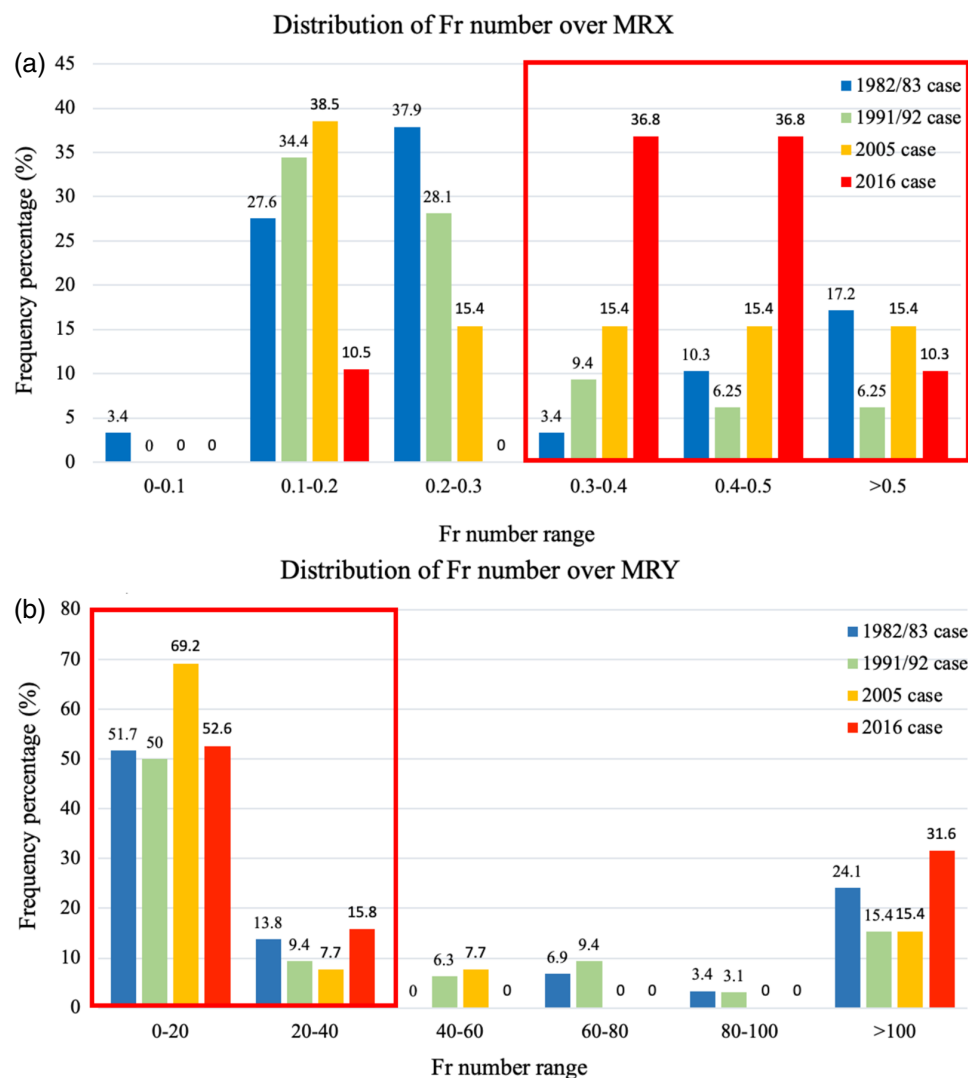


**FIGURE 13** The distribution of daily Froude numbers (Fr) over the MRX and MRY for all four melt cases. The number on top of each bar represent the percentage of certain Froude number range in the whole span. The red boxes highlight the range when sensible heat flux has a strong positive impact on surface melting [Colour figure can be viewed at [wileyonlinelibrary.com](http://wileyonlinelibrary.com)]

are similar, with strong moisture flux toward the eastern RIS and coastal MBL at the beginning of the event, which accounted for  $\sim 39$  and  $\sim 63\%$  of the melting period. On average, the 2005 case has larger amount of moisture imports during the melting period, however, the 2016 case has more intensified marine intrusions that are responsible for the spike in precipitation and RH (e.g., Figure 6c). Also, the correlation between moisture flux and surface melting over WA can be complicated with contributions from different mechanisms.

With abundant moisture imports, WA can experience significant impacts of low-level liquid clouds occurring frequently during the austral summer (December and January), especially for the RIS (Scott *et al.*, 2017). When the moisture flux intrudes into the eastern RIS directly from Ross Sea region (direct marine air advection), it can lead to extensive cloud cover, an increase in water vapor, and warmer air temperature, which can contribute to the extensive LWD over the coastal RIS and, sometimes, reaching the central RIS. As mentioned above, the

eastern RIS had an increase in LWD caused by low-level liquid clouds at the beginning of the 2016 case (Nicolas *et al.*, 2017). And at the beginning of the 2005 case and the peak of the 2016 case, the central RIS has an LWD around  $260\text{--}300\text{ W}\cdot\text{m}^{-2}$  (not shown), which benefits the expansion of the surface melting. The increase in LWD is also found along the coastal RIS, especially in the 1982/1983 and 1991/1992 cases. In brief, increasing LWD caused by the low-level liquid clouds and deep warm air column is usually responsible for the expansion of the surface melting over the coastal and middle RIS (Nicolas *et al.*, 2017; Hu *et al.*, 2019). Furthermore, sublimation from the melting surface favors cloud formation, as well as the melting expansion. However, the LWD can be compensated by the LWU if widespread surface melting occurred, such as the more negative  $\text{LW}_{\text{net}}$  in the 2016 case (Figure 4).

The West Antarctic continent is not the only region under the warming impact of the low-level liquid cloud. The Greenland Ice Sheet experienced widespread surface melting in July 2012 affected by liquid clouds, which were



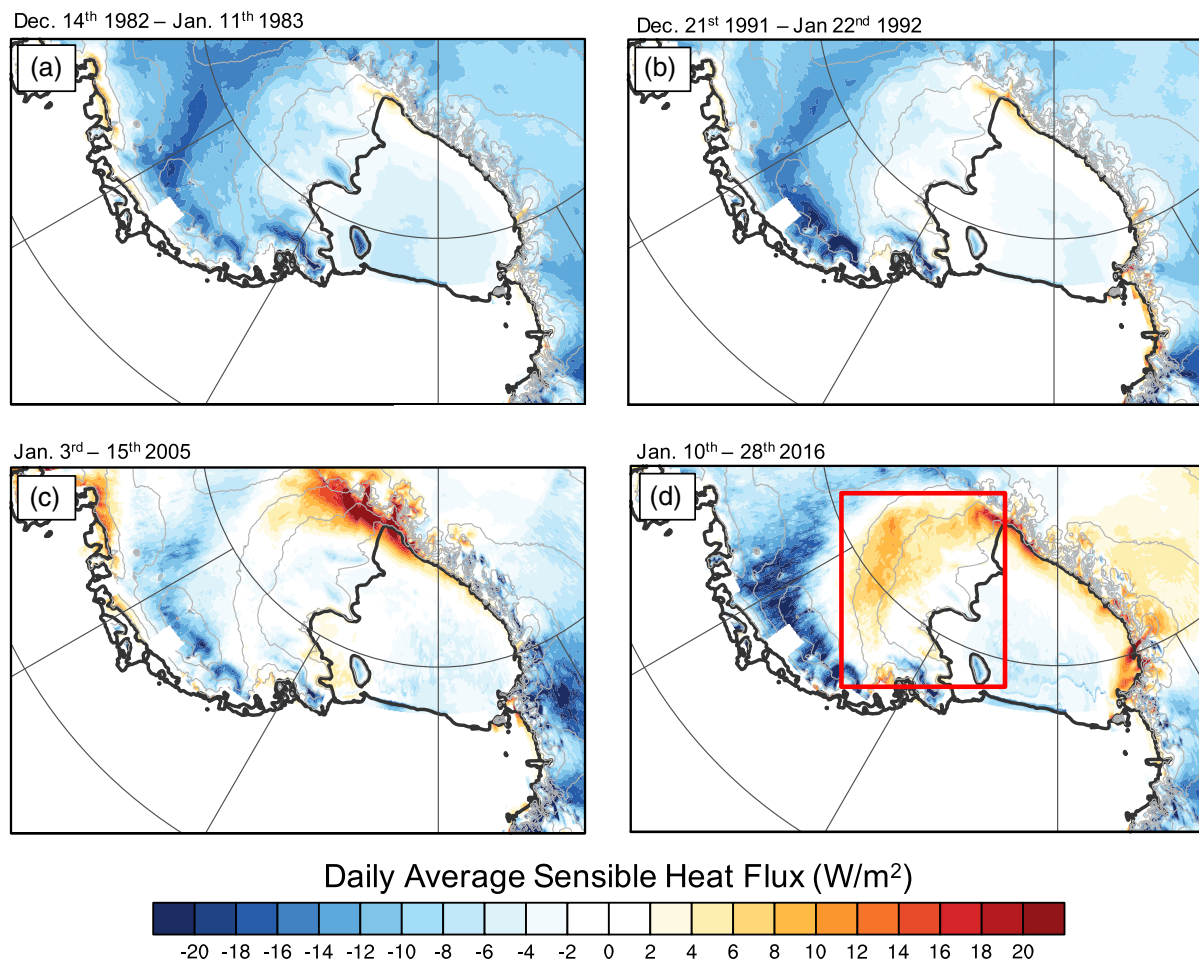


**FIGURE 14** The daily average of sensible heat flux from PWRP domain 2 outputs for four melt cases. The red rectangle indicates the area that has positive sensible heat flux [Colour figure can be viewed at [wileyonlinelibrary.com](http://wileyonlinelibrary.com)]

thick and low enough to enhance the LWD and optically thin enough to let sufficient solar radiation through (Bennartz *et al.*, 2013). On the Larsen C Ice Shelf in the AP, summertime cloud phase can dominate the SEB and thus control the occurrence of the melting (Lachlan-Cope *et al.*, 2016; Listowski *et al.*, 2019; Gilbert *et al.*, 2020). The formation of low liquid clouds depends on both regional flow patterns and synoptic-scale circulations (Silber *et al.*, 2019a). Also, a decline in sea-ice concentration can favor evaporation from the ocean to the lower troposphere and thus enhance formation of low-level liquid clouds (Scott *et al.*, 2019). Liquid water clouds have a critical impact on LWD and consequent surface melting. Thus, accurate model simulation and observations of clouds, especially for low-level liquid clouds, is necessary for future studies. A correct description of moisture imports, regional circulation patterns, and their modification by local topography is crucial for prediction of cloud impacts over WA.

Meanwhile, strong ARs over the AP can also amplify foehn warming through extra latent heat release and

potential clear sky conditions on the leeside (Bozkurt *et al.*, 2018). Over the RIS, a strong foehn effect dominated by the thermodynamic mechanism can be the lead driver of melting under clear sky conditions. For clear sky conditions to occur, it is necessary that sufficient moisture be transported toward mountain barriers by winds that move perpendicular to the ridges and are fast enough to climb over them. Thus, condensation can occur on the upwind side, resulting in warmer and drier air descending on the leeside. For melt cases in this article, when the moisture flux reaches the eastern RIS by crossing MRX over MBL, limited low-level air blocking and strong condensation occur on the upwind side, and thus the leeside is more likely to have foehn clearance. In this study, the 1982/1983 and 1991/1992 cases experience decreasing SWD with time, and the 2005 and 2016 cases are the opposite. The weaker foehn effect and moderate warm marine air intrusion in the first two cases led to more significant cloud impacts rather than clear sky conditions. However, with a stronger foehn effect, the 2005 and 2016 cases show a  $\sim 40 \text{ W}\cdot\text{m}^{-2}$  increase in SWD resulting from



foehn clearance at the beginning of the events, especially for the 2005 case (not shown). Clear sky conditions usually affect the Siple Coast and western MBL and contribute up to  $380 \text{ W} \cdot \text{m}^{-2}$  in SWD (not shown). This mechanism lets the surface melting develop further inland to western MBL. The intensified melting can also decrease the surface albedo and reduce the SWU, thus the  $\text{SW}_{\text{net}}$  contributes more to the melting as a positive feedback (e.g., 2016 case; Figure 4). Thus, the  $\text{SW}_{\text{net}}$ , as the dominating component in the SEB, usually increases with time (Figure 4). Similarly, the increasing SWD associated with the foehn effect can also enhance the melt rates, and accelerate the ice loss over the Larsen C Ice Shelf (e.g., Elvidge *et al.*, 2020).

In addition to the contribution of  $\text{SW}_{\text{net}}$  and  $\text{LW}_{\text{net}}$  to the SEB, SHF associated with foehn effect can be important to surface melting. The AP usually experiences a strong foehn effect and can have SHF-dominated surface melting (Elvidge and Renfrew, 2016; Datta *et al.*, 2019; Elvidge *et al.*, 2020). With stably stratified foehn conditions, low-level air is blocked and upper-level air with higher potential temperature can significantly warm the surface temperature via sensible heat transfer (Scorer, 1978; Elvidge *et al.*, 2020). Similarly in WA, a strong foehn effect induced a  $\sim 20 \text{ W} \cdot \text{m}^{-2}$  increase of SHF on the leeside of MRX and MRY (e.g., the 2016 case). Although the magnitude of SHF is much smaller than the SWD and LWD, it can warm the surface above the freezing point and thus trigger melting. Stronger mountain waves, such as rotors or cavities, are more likely to increase the SHF impact (Froude number  $\sim 1$ ). However, unlike the AP region, WA rarely experiences melt cases dominated by SHF due to its gentle and more complicated topography.

## 5 | SUMMARY

This article investigates four major melt events based on PWRP simulation driven by ERA5 reanalysis data with MODIS observed albedo (2005 and 2016 cases). Benefiting from the more advanced microphysical scheme (e.g., Morrison scheme), PWRP significantly improves the cloud simulation and related surface net radiation (Hines *et al.*, 2019). The descriptions of moisture imports from ERA5, precipitation from PWRP, and cloud conditions from CERES are consistent with each other. Also, compared with the BSRN station observations, PWRP provides reliable representation of SWD and LWD, with an average correlation coefficient of 0.88 and 0.69, respectively. In addition, the melt flux pattern calculated based on PWRP is consistent with cumulative melt days derived from passive microwave satellite data, especially for the 2016 case with MODIS albedo assimilation that further improves the simulation.

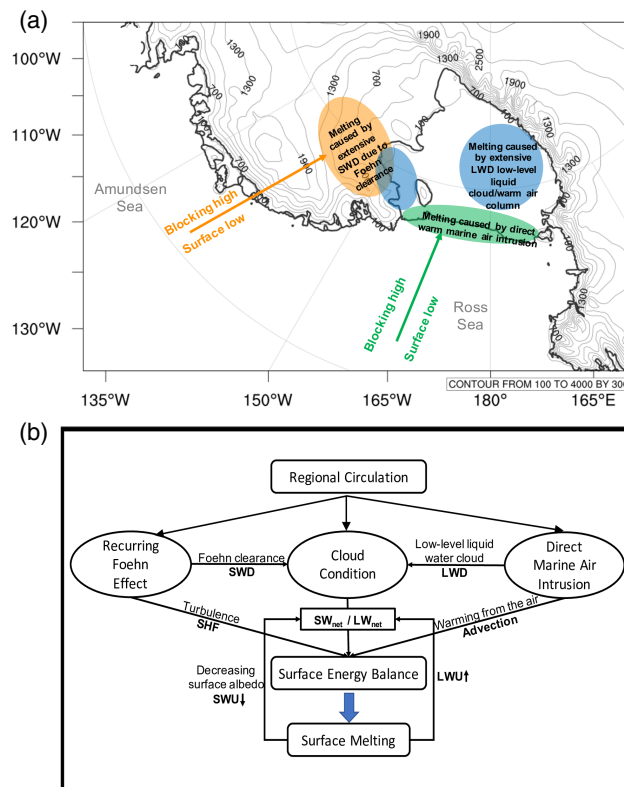


**FIGURE 15** (a) Regional factors causing surface melting over the Ross Ice Shelf (RIS); green and orange arrows represent the warm marine air advection; green, orange and blue shadow represent the melting areas driven by different regional factors; (b) schematic chart of regional factors for surface melting over the RIS, which reveals the relationship between each factor [Colour figure can be viewed at [wileyonlinelibrary.com](http://wileyonlinelibrary.com)]

Regional moisture imports significantly contribute to the surface melting over the RIS, which tends to occur more frequently and intensively in recent decades (Scott *et al.*, 2019; Zou *et al.*, 2019). This article concludes the regional factors from a SEB perspective as a complement to the effort of Zou *et al.* (2021). In general, with stronger moisture propagating inland toward MBL or the RIS, such as the 2005 and 2016 cases, the RIS is more likely to experience extensive and intensified surface melting. The dominant mechanism in each melt case varies, and different areas of the RIS are controlled by different regional drivers with interaction among them (Figure 15a).

The cloud cover over the RIS mainly depends on moisture transport from the Ross/Amundsen Sea region. For example, coastal RIS melting usually occurs when a blocking high is close to the Sulzberger Ice Shelf and a low-pressure center present in the Ross Sea. Sometimes, with strong moisture flux, the melting can extend to the proximity of the Siple Coast region. Based on the SEB analysis of these four melt cases, the middle, western,



and coastal RIS are more likely to have extensive melting due to an increase in LWD (up to  $80 \text{ W} \cdot \text{m}^{-2}$  in anomaly), which is associated with direct moisture import from the Amundsen/Ross Sea or sublimation from the wet surface and above freezing surface temperatures (Figure 15a). Either the formation of the low-level liquid clouds or the deep warm air column causes the LWD to increase (Nicolas *et al.*, 2017; Hu *et al.*, 2019). This mechanism is observed in all four melt cases, while the 1991/1992 case is mainly driven by the direct warm air advection that leads to significant coastal melting (Zou *et al.*, 2021). In general, this mechanism has less impact inland (e.g., western MBL) and tends to result in mild and prolonged melting.

In contrast, western MBL usually has surface warming due to the increase in SWD (up to  $48 \text{ W} \cdot \text{m}^{-2}$  in anomaly), which is caused by foehn clearance on the leeside of mountain ranges (Figures 4, 10, and 11; e.g., 2005 and 2016 cases). With the blocking high located over the coastal MBL ( $120\text{--}150^\circ \text{ W}$ ) and strong moisture imports from the Amundsen Sea blowing nearly perpendicularly toward MBL, intensified precipitation on the upwind side is captured in both the 2005 and 2016 cases (Zou *et al.*, 2021). Both CERES data and PWRP output show clear sky condition over Siple Coast and western MBL during the melting period that correlated with the magnitude of the foehn effect. The 2005 and 2016 cases are dominated by this pattern and, consequently, have more intensified and short-lived melting (with fewer days) compared with the 1991/1992 and 1982/1983 cases. Also, the decreasing surface albedo caused by melting reduces the SWU and further increases the  $\text{SW}_{\text{net}}$  that accelerates the melting. In the 2016 case, these combined impacts contribute to a  $\sim 60 \text{ W} \cdot \text{m}^{-2}$   $\text{SW}_{\text{net}}$  increase after January 21 (Figure 4).

Even though the surface net radiation dominates the SEB over the RIS, SHF is also a significant contributor to the surface warming, especially in the 2005 and 2016 cases, which leads to a  $\sim 20 \text{ W} \cdot \text{m}^{-2}$  increase over the leeside of MRX and MRY. With stronger and more frequent foehn effect (Zou *et al.*, 2021), the 2005 and 2016 cases are more likely to have sensible heat transfer from upper foehn flow to the ground. The Froude number is calculated to build the connection between mountain waves and efficient sensible heat transfer. When the Froude number is closer to or slightly larger than 1, the heat is transferred from foehn flow to the ground more effectively, contributing to surface melting. However, if the Froude number is much smaller than 1, the upper warm flow is unable to penetrate the near surface air and reach the ground. And, if the Froude number is close to infinity, the breaking waves and irregular turbulence seem to hamper efficient sensible heat transfer.

## 6 | CONCLUSIONS

Based on the comprehensive investigation of four major melt events (Part I and II), two conclusions can be drawn. First, recurring foehn warming, direct marine air intrusion, and cloud impacts play significant roles in previous major melt cases (Figure 15b). Also, warm air advection and foehn effect can affect cloud conditions via moisture import and foehn clearance. With the exception of the 1982/1983 case, all other cases presented experience foehn warming for around half of the melting period, and have moisture import from the ocean that contributed to the cloud formation for more than 30% of the melting period (Zou *et al.*, 2021, Table 3). The melting induced by the foehn effect starts at the eastern RIS and slowly expands to the middle of the RIS, as well as western MBL. Without a strong foehn effect over MRX, the RIS rarely has extensive surface melting reaching the Queen Maud Range, Transantarctic Mountains (e.g., 1991/1992 case). On the one hand, the marine air propagation from the Amundsen Sea to coastal MBL can amplify the foehn warming via condensation on the upwind side and extensive SWD on the leeside. The widespread melting can further amplify  $\text{SW}_{\text{net}}$  via reducing SWU. On the other hand, the direct moist and warm air intrusion from the Ross Sea not only warms the coastal RIS but also expands the melting to the middle RIS with extra LWD from low-level liquid clouds and deep warm air column. In brief, low-level liquid clouds dominate the surface melting over the coastal and middle RIS, and clear sky conditions control the eastern RIS and western MBL. Taking the melting area as a whole, the  $\text{SW}_{\text{net}}$  is the leading component in the SEB for all the melt cases. In addition, the foehn effect can also enhance the turbulence that leads to a moderate SHF increase.

Second, this study further emphasizes the importance of accurate descriptions of regional circulations, surface conditions, and cloud impacts for surface melting analysis over WA. Studying the melt cases from an SEB aspect provides a more comprehensive explanation of the melting mechanisms. For future research, improvements in cloud prediction over WA are necessary. Also, an algorithm in the land surface model should be included to predict the surface albedo as a function of snow surface conditions. Nudging toward MODIS observed albedo can ensure the predicted albedo remains realistic. In addition, the prediction of the stability of West Antarctic ice shelves should not only consider the large-scale climatic modes but also regional drivers.

## ACKNOWLEDGMENT

This research was supported by National Science Foundation grants PLR1443443, PLR1341695, and 1823135, and is a contribution to the Year of Polar Prediction (YOPP)



initiated by the World Weather Research Programme (WWRP). Contribution number 1608 of Byrd Polar and Climate Research Center. We thank Johan Booth and Matthew Lazzara for providing additional information on BSRN observations. Also, Xun Zou appreciates the Presidential Fellowship awarded by The Ohio State University and the financial support provided by the Department of Geography during her PhD study.


## AUTHOR CONTRIBUTIONS

**Xun Zou:** Conceptualization; data curation; formal analysis; investigation; methodology; validation; visualization; writing-original draft; writing-review & editing.


**David Bromwich:** Conceptualization; formal analysis; funding acquisition; project administration; supervision; writing-review & editing. **Alvaro Montenegro:** Supervision; writing-review & editing. **Sheng-Hung Wang:** Data curation; software; writing-review & editing. **Le-Sheng Bai:** Data curation; software.

## ORCID

Xun Zou  <https://orcid.org/0000-0003-1620-3198>

David H. Bromwich  <https://orcid.org/0000-0003-4608-8071>

Alvaro Montenegro  <https://orcid.org/0000-0001-6848-1996>

Sheng-Hung Wang  <https://orcid.org/0000-0002-8057-835X>

## REFERENCES

- Barrett, A.I., Hogan, R.J. and Forbes, R.M. (2017) Why are mixed-phase altocumulus clouds poorly predicted by large-scale models? Part 2. Vertical resolution sensitivity and parameterization. *Journal of Geophysical Research – Atmospheres*, 122, 9927–9944. <https://doi.org/10.1002/2016JD026322>.
- Bennartz, R., Shupe, M.D., Turner, D.D., Walden, V.P., Steffen, K., Cox, C.J., Kulie, M.S., Miller, N.B. and Pettersen, C. (2013) July 2012 Greenland melt extent enhanced by low-level liquid clouds. *Nature*, 496, 83–86. <https://doi.org/10.1038/nature12002>.
- Bozkurt, D., Bromwich, D.H., Carrasco, J., Hines, K.M., Maureira, J.C. and Rondanelli, R. (2020) Recent near-surface temperature trends in the Antarctic Peninsula from observed, reanalysis and regional climate model data. *Advances in Atmospheric Sciences*, 37, 477–493. <https://doi.org/10.1007/s00376-020-9183-x>.
- Bozkurt, D., Rondanelli, R., Marín, J.C. and Garreaud, R. (2018) Foehn event triggered by an atmospheric river underlies record-setting temperature along continental Antarctica. *Journal of Geophysical Research – Atmospheres*, 123, 3871–3892. <https://doi.org/10.1002/2017JD027796>.
- Bromwich, D.H., Otieno, F.O., Hines, K.M., Manning, K.W. and Shilo, E. (2013) Comprehensive evaluation of polar weather research and forecasting model performance in the Antarctic. *Journal of Geophysical Research – Atmospheres*, 118, 274–292. <https://doi.org/10.1029/2012JD018139>.
- Cape, M.R., Vernet, M., Skvarca, P., Marinsek, S., Scambos, T. and Domack, E. (2015) Foehn winds link climate-driven warming to ice shelf evolution in Antarctica. *Journal of Geophysical Research – Atmospheres*, 120, 2015JD023465. <https://doi.org/10.1002/2015JD023465>.
- Datta, R.T., Tedesco, M., Fettweis, X., Agosta, C., Lhermitte, S., Lenaerts, J.T.M. and Wever, N. (2019) The effect of foehn-induced surface melt on firn evolution over the northeast Antarctic Peninsula. *Geophysical Research Letters*, 46, 3822–3831. <https://doi.org/10.1029/2018GL080845>.
- Driemel, A., Augustine, J., Behrens, K., Colle, S., Cox, C., Cuevas-Agulló, E., Denn, F.M., Duprat, T., Fukuda, M., Grobe, H., Haeffelin, M., Hodges, G., Hyett, N., Ijima, O., Kallis, A., Knap, W., Kustov, V., Long, C.N., Longenecker, D., Lupi, A., Maturilli, M., Mimouni, M., Ntsangwane, L., Ogihara, H., Olano, X., Olefs, M., Omori, M., Passamani, L., Pereira, E.B., Schmithüsen, H., Schumacher, S., Sieger, R., Tamlyn, J., Vogt, R., Vuilleumier, L., Xia, X., Ohmura, A. and König-Langlo, G. (2018) Baseline surface radiation network (BSRN) structure and data description (1992–2017). *Earth System Science Data*, 10, 1491–1501. <https://doi.org/10.5194/essd-10-1491-2018>.
- Durrán, D.R. (1990) Mountain waves and downslope winds. In: Banta, R.M., Berri, G., Blumen, W., Carruthers, D.J., Dalu, G.A., Durrán, D.R., Egger, J., Garratt, J.R., Hanna, S.R., Hunt, J.C.R., Meroney, R.N., Miller, W., Neff, W.D., Nicolini, M., Paegle, J., Pielke, R.A., Smith, R.B., Strimaitis, D.G., Vukicevic, T., Whitman, C.D. and Blumen, W. (Eds.) *Atmospheric Processes over Complex Terrain*. Boston, MA: American Meteorological Society, pp. 59–81.
- Elvidge, A.D., Munneke, P.K., King, J.C., Renfrew, I.A. and Gilbert, E. (2020) Atmospheric drivers of melt on Larsen C ice shelf: surface energy budget regimes and the impact of foehn. *Journal of Geophysical Research – Atmospheres*, 125, e2020JD032463. <https://doi.org/10.1029/2020JD032463>.
- Elvidge, A.D. and Renfrew, I.A. (2016) The causes of foehn warming in the lee of mountains. *Bulletin of the American Meteorological Society*, 97(3), 455–466. <https://doi.org/10.1175/BAMS-D-14-00194.1>.
- Fréville, H., Brun, E., Picard, G., Tatarinova, N., Arnaud, L., Lanconelli, C., Reijmer, C. and van den Broeke, M. (2014) Using MODIS land surface temperatures and the Crocus snow model to understand the warm bias of ERA-Interim reanalyses at the surface in Antarctica. *The Cryosphere*, 8, 1361–1373. <https://doi.org/10.5194/tc-8-1361-2014>.
- Ghiz, M.L., Scott, R.C., Vogelmann, A.M., Lenaerts, J.T.M., Lazzara, M. and Lubin, D. (2020) Energetics of surface melt in West Antarctica. *The Cryosphere Discussions*, 1–42. <https://doi.org/10.5194/tc-2020-311>.
- Gilbert, E., Orr, A., King, J.C., Renfrew, I.A., Lachlan-Cope, T., Field, P.F. and Boutle, I.A. (2020) Summertime cloud phase strongly influences surface melting on the Larsen C ice shelf, Antarctica. *Quarterly Journal of the Royal Meteorological Society*, 146, 1575–1589. <https://doi.org/10.1002/qj.3753>.
- Gorodetskaya, I.V., Silva, T., Schmithüsen, H. and Hirasawa, N. (2020) Atmospheric river signatures in radiosonde profiles and reanalyses at the Dronning Maud Land coast, East Antarctica. *Advances in Atmospheric Sciences*, 37, 455–476. <https://doi.org/10.1007/s00376-020-9221-8>.
- Grosvenor, D.P., King, J.C., Choularton, T.W. and Lachlan-Cope, T. (2014) Downslope föhn winds over the Antarctic Peninsula



- and their effect on the Larsen ice shelves. *Atmospheric Chemistry and Physics*, 14, 9481–9509. <https://doi.org/10.5194/acp-14-9481-2014>.
- Hersbach, H., Bell, B., Berrisford, P., Hirahara, S., Horányi, A., Muñoz-Sabater, J., Nicolas, J., Peubey, C., Radu, R., Schepers, D., Simmons, A., Soci, C., Abdalla, S., Abellan, X., Balsamo, G., Bechtold, P., Biavati, G., Bidlot, J., Bonavita, M., Chiara, G.D., Dahlgren, P., Dee, D., Diamantakis, M., Dragani, R., Flemming, J., Forbes, R., Fuentes, M., Geer, A., Haimberger, L., Healy, S., Hogan, R.J., Hólm, E., Janisková, M., Keeley, S., Laloyaux, P., Lopez, P., Lupu, C., Radnoti, G., de Rosnay, P., Rozum, I., Vamborg, F., Villaume, S. and Thépaut, J.-N. (2020) The ERA5 global reanalysis. *Quarterly Journal of the Royal Meteorological Society*, 146, 1999–2049. <https://doi.org/10.1002/qj.3803>.
- Hines, K.M. and Bromwich, D.H. (2008) Development and testing of polar weather research and forecasting (WRF) model. Part I: Greenland ice sheet meteorology. *Monthly Weather Review*, 136, 1971–1989. <https://doi.org/10.1175/2007MWR2112.1>.
- Hines, K.M., Bromwich, D.H., Wang, S.-H., Silber, I., Verlinde, J. and Lubin, D. (2019) Microphysics of summer clouds in central West Antarctica simulated by polar WRF and AMPS. *Atmospheric Chemistry and Physics*, 19, 12431–12454. <https://doi.org/10.5194/acp-19-12431-2019>.
- Hoffman, M.J., Fountain, A.G. and Liston, G.E. (2008) Surface energy balance and melt thresholds over 11 years at Taylor Glacier, Antarctica. *Journal of Geophysical Research: Earth Surface*, 113, F04014. <https://doi.org/10.1029/2008JF001029>.
- Hogan, R.J., Francis, P.N., Flentje, H., Illingworth, A.J., Quante, M. and Pelon, J. (2003) Characteristics of mixed-phase clouds. I: Lidar, radar and aircraft observations from CLARE'98. *Quarterly Journal of the Royal Meteorological Society*, 129, 2089–2116. <https://doi.org/10.1256/rj.01.208>.
- Hu, X., Sejas, S.A., Cai, M., Li, Z. and Yang, S. (2019) Atmospheric dynamics footprint on the January 2016 ice sheet melting in West Antarctica. *Geophysical Research Letters*, 46, 2829–2835. <https://doi.org/10.1029/2018GL081374>.
- King, J.C., Kirchaessner, A., Bevan, S., Elvidge, A.D., Kuipers Munneke, P., Luckman, A., Orr, A., Renfrew, I.A. and van den Broeke, M.R. (2017) The impact of föhn winds on surface energy balance during the 2010–11 melt season over Larsen C ice shelf, Antarctica. *Journal of Geophysical Research – Atmospheres*, 122, 12062–12076. <https://doi.org/10.1002/2017JD026809>.
- Lachlan-Cope, T., Listowski, C. and O'Shea, S. (2016) The microphysics of clouds over the Antarctic peninsula – part 1: observations. *Atmospheric Chemistry and Physics*, 16, 15605–15617. <https://doi.org/10.5194/acp-16-15605-2016>.
- Listowski, C., Delanoë, J., Kirchaessner, A., Lachlan-Cope, T. and King, J. (2019) Antarctic clouds, supercooled liquid water and mixed phase, investigated with DARDAR: geographical and seasonal variations. *Atmospheric Chemistry and Physics*, 19, 6771–6808. <https://doi.org/10.5194/acp-19-6771-2019>.
- Listowski, C. and Lachlan-Cope, T. (2017) The microphysics of clouds over the Antarctic peninsula – part 2: modelling aspects within polar WRF. *Atmospheric Chemistry and Physics*, 17, 10195–10221. <https://doi.org/10.5194/acp-17-10195-2017>.
- Loeb, N.G., Doelling, D.R., Wang, H., Su, W., Nguyen, C., Corbett, J.G., Liang, L., Mitrescu, C., Rose, F.G. and Kato, S. (2017) Clouds and the Earth's radiant energy system (CERES) energy balanced and filled (EBAF) top-of-atmosphere (TOA) edition-4.0 data product. *Journal of Climate*, 31, 895–918. <https://doi.org/10.1175/JCLI-D-17-0208.1>.
- Marshall, G.J., Orr, A., van Lipzig, N.P.M. and King, J.C. (2006) The impact of a changing southern hemisphere annular mode on Antarctic peninsula summer temperatures. *Journal of Climate*, 19, 5388–5404. <https://doi.org/10.1175/JCLI3844.1>.
- Mattingly, K.S., Mote, T.L. and Fettweis, X. (2018) Atmospheric river impacts on Greenland Ice Sheet surface mass balance. *Journal of Geophysical Research: Atmospheres*, 123, 8538–8560. <https://doi.org/10.1029/2018JD028714>.
- Meng, X., Lyu, S., Zhang, T., Zhao, L., Li, Z., Han, B., Li, S., Ma, D., Chen, H., Ao, Y., Luo, S., Shen, Y., Guo, J. and Wen, L. (2018) Simulated cold bias being improved by using MODIS time-varying albedo in the Tibetan plateau in WRF model. *Environmental Research Letters*, 13, 044028. <https://doi.org/10.1088/1748-9326/aab44a>.
- Miltenberger, A.K., Reynolds, S. and Sprenger, M. (2016) Revisiting the latent heating contribution to föhn warming: Lagrangian analysis of two föhn events over the Swiss Alps. *Quarterly Journal of the Royal Meteorological Society*, 142, 2194–2204. <https://doi.org/10.1002/qj.2816>.
- Morcrette, J.J., Barker, H.W., Cole, J.N.S., Iacono, M.J. and Pincus, R. (2008) Impact of a new radiation package, McRad, in the ECMWF integrated forecasting system. *Monthly Weather Review*, 136, 4773–4798. <https://doi.org/10.1175/2008MWR2363.1>.
- Morrison, H., Curry, J.A. and Khvorostyanov, V.I. (2005) A new double-moment microphysics parameterization for application in cloud and climate models. Part I: description. *Journal of the Atmospheric Sciences*, 62, 1665–1677. <https://doi.org/10.1175/JAS3446.1>.
- Morrison, H., Thompson, G. and Tatarskii, V. (2009) Impact of cloud microphysics on the development of trailing stratiform precipitation in a simulated squall line: comparison of one- and two-moment schemes. *Monthly Weather Review*, 137, 991–1007. <https://doi.org/10.1175/2008MWR2556.1>.
- Nakanishi, M. and Niino, H. (2004) An improved Mellor–Yamada level-3 model with condensation physics: its design and verification. *Boundary-Layer Meteorology*, 112, 1–31. <https://doi.org/10.1023/B:BOUN.0000020164.04146.98>.
- Nicolas, J. (2018) “Antarctic daily surface melt data estimated from SMMR, SSM/I, and SSMIS passive microwave observations, 1978–2016.” Polar Data Centre, Natural Environment Research Council, UK. <https://doi.org/10.5285/FFD24DD7-E201-4A02-923F-038680BF7BB5>.
- Nicolas, J.P., Vogelmann, A.M., Scott, R.C., Wilson, A.B., Cadetdu, M.P., Bromwich, D.H., Verlinde, J., Lubin, D., Russell, L.M., Jenkinson, C., Powers, H.H., Ryzek, M., Stone, G. and Wille, J.D. (2017) January 2016 extensive summer melt in West Antarctica favoured by strong El Niño. *Nature Communications*, 8, 15799. <https://doi.org/10.1038/ncomms15799>.
- Ohmura, A., Dutton, E.G., Forgan, B., Fröhlich, C., Gilgen, H., Heger, H., Heimo, A., König-Langlo, G., McArthur, B., Müller, G., Philipona, R., Pinker, R., Whitlock, C.H., Dehne, K. and Wild, M. (1998) Baseline surface radiation network (BSRN/WCRP): new precision radiometry for climate research. *Bulletin of the American Meteorological Society*, 79, 2115–2136. [https://doi.org/10.1175/1520-0477\(1998\)079<2115:BSRNBW>2.0.CO;2](https://doi.org/10.1175/1520-0477(1998)079<2115:BSRNBW>2.0.CO;2).
- Powers, J.G., Manning, K.W., Bromwich, D.H., Cassano, J.J. and Cayette, A.M. (2012) A decade of Antarctic science support



- through AMPS. *Bulletin of the American Meteorological Society*, 93, 1699–1712. <https://doi.org/10.1175/BAMS-D-11-00186.1>.
- Roesch, A., Wild, M., Ohmura, A., Dutton, E.G., Long, C.N. and Zhang, T. (2011) Assessment of BSRN radiation records for the computation of monthly means. *Atmospheric Measurement Techniques*, 4, 339–354. <https://doi.org/10.5194/amt-4-339-2011>.
- Rutan, D.A., Kato, S., Doelling, D.R., Rose, F.G., Nguyen, L.T., Caldwell, T.E. and Loeb, N.G. (2015) CERES synoptic product: methodology and validation of surface radiant flux. *Journal of Atmospheric and Oceanic Technology*, 32, 1121–1143. <https://doi.org/10.1175/JTECH-D-14-00165.1>.
- Schaaf, C. and Wang, Z. (2015). MCD43C3 MODIS/Terra+Aqua BRDF/Albedo Albedo Daily L3 Global 0.05Deg CMG V006 [Data set]. NASA EOSDIS Land Processes DAAC. Accessed December 16, 2020. <https://doi.org/10.5067/MODIS/MCD43C3.006>
- Scorer, R.S. (1978) *Environmental Aerodynamics*. Australia: Halsted Press, p. 488.
- Scott, R.C., Lubin, D., Vogelmann, A.M. and Kato, S. (2017) West Antarctic ice sheet cloud cover and surface radiation budget from NASA A-Train satellites. *Journal of Climate*, 30, 6151–6170. <https://doi.org/10.1175/JCLI-D-16-0644.1>.
- Scott, R.C., Nicolas, J.P., Bromwich, D.H., Norris, J.R. and Lubin, D. (2019) Meteorological drivers and large-scale climate forcing of West Antarctic surface melt. *Journal of Climate*, 32, 665–684. <https://doi.org/10.1175/JCLI-D-18-0233.1>.
- Silber, I., Verlinde, J., Cadeddu, M., Flynn, C.J., Vogelmann, A.M. and Eloranta, E.W. (2019a) Antarctic cloud macrophysical, thermodynamic phase, and atmospheric inversion coupling properties at McMurdo station—Part II: radiative impact during different synoptic regimes. *Journal of Geophysical Research – Atmospheres*, 124, 1697–1719. <https://doi.org/10.1029/2018JD029471>.
- Silber, I., Verlinde, J., Wang, S.-H., Bromwich, D.H., Fridlind, A.M., Cadeddu, M., Eloranta, E.W. and Flynn, C.J. (2019b) Cloud influence on ERA5 and AMPS surface downwelling longwave radiation biases in West Antarctica. *Journal of Climate*, 32, 7935–7949. <https://doi.org/10.1175/JCLI-D-19-0149.1>.
- Song, R., Muller, J.-P., Kharbouche, S. and Woodgate, W. (2019) Intercomparison of surface albedo retrievals from MISR, MODIS, CGLS using tower and upscaled tower measurements. *Remote Sensing*, 11, 644. <https://doi.org/10.3390/rs11060644>.
- Speirs, J.C., McGowan, H.A., Steinhoff, D.F. and Bromwich, D.H. (2013) Regional climate variability driven by foehn winds in the McMurdo Dry Valleys, Antarctica. *International Journal of Climatology*, 33, 945–958. <https://doi.org/10.1002/joc.3481>.
- Steinhoff, D.F., Bromwich, D.H. and Monaghan, A. (2013) Dynamics of the foehn mechanism in the McMurdo dry valleys of Antarctica from Polar WRF. *Quarterly Journal of the Royal Meteorological Society*, 139, 1615–1631. <https://doi.org/10.1002/qj.2038>.
- Steinhoff, D.F., Bromwich, D.H., Speirs, J.C., McGowan, H.A. and Monaghan, A.J. (2014) Austral summer Foehn winds over the McMurdo Dry Valleys of Antarctica from polar WRF. *Quarterly Journal of the Royal Meteorological Society*, 140, 1825–1837. <https://doi.org/10.1002/qj.2278>.
- Tiedtke, M. (1993) Representation of clouds in large-scale models. *Monthly Weather Review*, 121, 3040–3061. [https://doi.org/10.1175/1520-0493\(1993\)121<3040:ROCILS>2.0.CO;2](https://doi.org/10.1175/1520-0493(1993)121<3040:ROCILS>2.0.CO;2).
- van den Broeke, M., Reijmer, C., Van As, D. and Boot, W. (2006) Daily cycle of the surface energy balance in Antarctica and the influence of clouds. *International Journal of Climatology*, 26, 1587–1605. <https://doi.org/10.1002/joc.1323>.
- Wild, M. (2008) Short-wave and long-wave surface radiation budgets in GCMs: a review based on the IPCC-AR4/CMIP3 models. *Tellus A: Dynamic Meteorology and Oceanography*, 60, 932–945. <https://doi.org/10.1111/j.1600-0870.2008.00342.x>.
- Wille, J.D., Bromwich, D.H., Nigro, M., Cassano, J., Mateling, M., Lazzara, M. and Wang, S.-H. (2016) Evaluation of the AMPS boundary layer simulations on the Ross Ice Shelf with tower observations. *Journal of Applied Meteorology and Climatology*, 55, 2349–2367. <https://doi.org/10.1175/JAMC-D-16-0032.1>.
- Wille, J.D., Favier, V., Dufour, A., Gorodetskaya, I.V., Turner, J., Agosta, C. and Codron, F. (2019) West Antarctic surface melt triggered by atmospheric rivers. *Nature Geoscience*, 12, 911–916. <https://doi.org/10.1038/s41561-019-0460-1>.
- Zhang, T., Stamnes, K. and Bowling, S.A. (1996) Impact of clouds on surface radiative fluxes and snowmelt in the Arctic and subarctic. *Journal of Climate*, 9, 2110–2123. [https://doi.org/10.1175/1520-0442\(1996\)009<2110:IOCOSR>2.0.CO;2](https://doi.org/10.1175/1520-0442(1996)009<2110:IOCOSR>2.0.CO;2).
- Zou, X., Bromwich, D.H., Nicolas, J.P., Montenegro, A. and Wang, S.-H. (2019) West Antarctic surface melt event of January 2016 facilitated by föhn warming. *Quarterly Journal of the Royal Meteorological Society*, 145, 687–704. <https://doi.org/10.1002/qj.3460>.
- Zou, X., Bromwich, D.H., Montenegro, A., Wang, S.-H. and Bai, L.-S. (2021) Major surface melting over the Ross ice shelf part I: Foehn effect. *Quarterly Journal of the Royal Meteorological Society*. <https://doi.org/10.1002/qj.4104>.

## SUPPORTING INFORMATION

Additional supporting information may be found online in the Supporting Information section at the end of this article.

**How to cite this article:** Zou, X., Bromwich, D.H., Montenegro, A., Wang, S.-H. & Bai, L. (2021) Major surface melting over the Ross Ice Shelf part II: Surface energy balance. *Quarterly Journal of the Royal Meteorological Society*, 147(738), 2895–2916. Available from: <https://doi.org/10.1002/qj.4105>